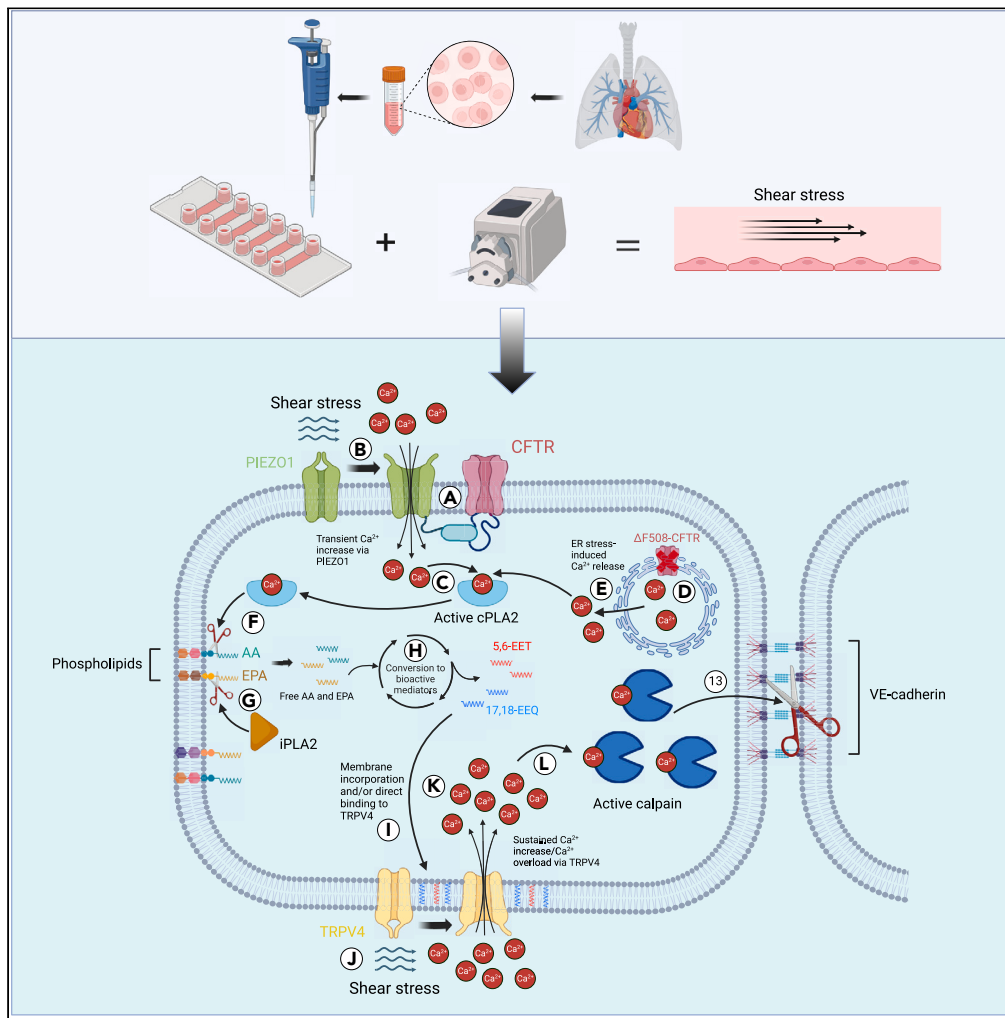## Article

Defective CFTR modulates mechanosensitive channels TRPV4 and PIEZO1 and drives endothelial barrier failure

Jean-Pierre Amoakon, Jesun Lee, Pramodha Liyanage, ..., Goutham Mylavarapu, Raouf Amin, Anjaparavanda P. Naren

amoakoja@mail.uc.edu (J.-P.A.)
apnaren@cshs.org (A.P.N.)

Highlights

CFTR deficiency promotes barrier failure in the pulmonary microvascular endothelium

CFTR deficiency alters endothelial cells lipid metabolism and membrane fluidity

CFTR deficiency sensitizes TRPV4 to fluid shear stress

CFTR directly interacts with PIEZO1

iScience

Article

Defective CFTR modulates mechanosensitive channels TRPV4 and PIEZO1 and drives endothelial barrier failure

Jean-Pierre Amoakon,[1,2,*] Jesun Lee,[2] Pramodha Liyanage,[2] Kavisha Arora,[2] Anja Karlstaedt,[3] Goutham Mylavarapu,[4] Raouf Amin,[4] and Anjaparavanda P. Naren.[1,2,4,5,*]

SUMMARY

Cystic fibrosis (CF) is a genetic disease caused by a mutation in the cystic fibrosis transmembrane conductance regulator (CFTR) gene. Despite reports of CFTR expression on endothelial cells, pulmonary vascular perturbations, and perfusion deficits in CF patients, the mechanism of pulmonary vascular disease in CF remains unclear. Here, our pilot study of 40 CF patients reveals a loss of small pulmonary blood vessels in patients with severe lung disease. Using a vessel-on-a-chip model, we establish a shear-stress-dependent mechanism of endothelial barrier failure in CF involving TRPV4, a mechanosensitive channel. Furthermore, we demonstrate that CFTR deficiency downregulates the function of PIEZO1, another mechanosensitive channel involved in angiogenesis and wound repair, and exacerbates loss of small pulmonary blood vessel. We also show that CFTR directly interacts with PIEZO1 and enhances its function. Our study identifies key cellular targets to mitigate loss of small pulmonary blood vessels in CF.

INTRODUCTION

Cystic fibrosis (CF) is a life-threatening genetic disorder caused by a deleterious mutation in the cystic fibrosis transmembrane conductance regulator (CFTR) gene. The CFTR protein is a cAMP-dependent chloride channel that is highly expressed in epithelial cells lining the lungs, the digestive tract, and reproductive organs.[1] Respiratory failure is the main cause of mortality in CF and often results from the collective effects of alveolar mucus plugging, lung fibrosis, chronic inflammation, progressive destruction of the structural airway, and poor ventilation.

The pathophysiology underlying CF lung disease may be related to multiple underlying processes. Historically, pathology in the airway epithelium has been of particular interest. However, The CFTR protein is also expressed on endothelial cells (ECs), among other cell types.[2] Available studies indicate that endothelial cell dysfunction plays a role in vascular pathology and perfusion deficits.[3–6] Sub-optimal gas exchange in the alveoli may also occur if endothelial cells in the pulmonary capillaries do not function normally, precluding adequate oxygenation.[7,8] Consequently, endothelial cell dysfunction may contribute to CF lung disease; yet the role of CFTR in endothelial cells within the pulmonary vasculature is not fully understood.

Endothelial cells are constantly subject to shear stress (SS), which is one of the most important external stimuli for endothelial homeostasis.[9–13] Small pulmonary blood vessels (SPBVs) must withstand physiologically high SS.[14,15] In non-CF lung diseases, such as emphysema and other obstructive pulmonary diseases, pulmonary vascular remodeling and pruning of SPBVs occurs; these changes coincide with reduced CFTR expression and blood flow changes.[16–23] This association suggests CFTR may play a role in microvascular homeostasis. Therefore, we set out to investigate how CFTR dysfunction affects the response of ECs to SS in the lung microvasculature using a vessel-on-a-chip model.[24]

We demonstrate that dysfunctional CFTR leads to loss of SPBVs by promoting endothelial barrier failure and impairing angiogenesis and wound repair. We identify a clear mechanism of endothelial barrier failure that is SS dependent and that involves TRPV4, a calcium-permeable mechanosensitive channel (MsC), and its associated downstream calcium signaling. Furthermore, we show that CFTR deficiency negatively affects the function of PIEZO1, another calcium-permeable MsC that is known to play a role in angiogenesis and wound repair,[25–27] two processes that can mitigate loss of SPBVs. We present evidence that CFTR directly interacts with and enhances the function of PIEZO1 and that CFTR deficiency reduces PIEZO1 channel activity. Overall, we establish previously unknown mechanisms underlying the progression of CF vascular disease and identify key cellular targets relevant to the loss of SPBVs in CF.

[1]Department of Systems Biology and Physiology, University of Cincinnati College of Medicine, Cincinnati, OH, USA
[2]Division of Pulmonary Medicine and Critical Care, Cedars-Sinai Medical Center, Los Angeles, CA, USA
[3]Department of Cardiology, Smidt Heart Institute, Cedars-Sinai Medical Center, Los Angeles, CA, USA
[4]Division of Pulmonary Medicine, Cincinnati Children's Hospital Medical Center, Cincinnati, OH, USA
[5]Lead contact
*Correspondence: amoakoja@mail.uc.edu (J.-P.A.), apnaren@cshs.org (A.P.N.)
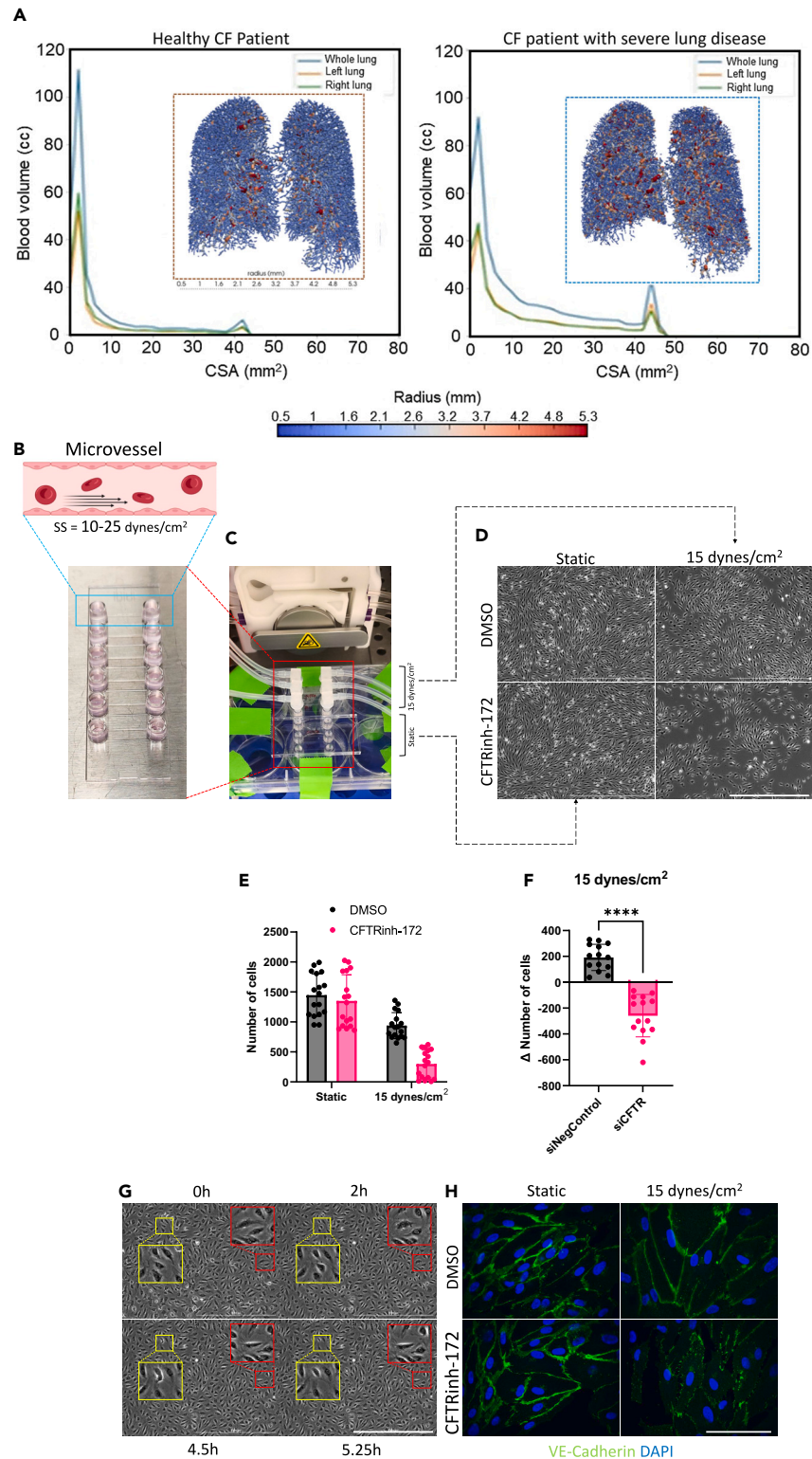https://doi.org/10.1016/j.isci.2024.110703

Figure 1. Shear stress stimulation on CFTR-defective lung microvascular ECs leads to loss of endothelial monolayer integrity

(A) Representative images of reconstructed pulmonary vasculatures of CF patients using pulmonary vascular morphometry extracted from volumetric computed tomography scans of the chest at maximum inspiration ($n > 10$ patients).

Figure 1. Continued

(B and C) Multi-channel vessel-on-a-chip microfluidic device (B) connected to a peristaltic pump for shear flow studies (C). Shear stress (SS) ranges from 10 to 25 dyne/cm^2 in the microvasculature.[15,28] Some of the channels remain in static conditions as controls for each treatment (C).

(D) Representative images used to quantify data in (E) (scale bar, 1,000 μm). Human lung microvascular ECs (HMVEC-Ls) were treated with DMSO or 20 μM CFTRinh-172. For each treatment, cells remained in static conditions or were subjected to SS (15 dyne/cm^2) for 24 h.

(E) Cell counts per image of DMSO and CFTRinh-172-treated HMVEC-Ls in static or flow conditions (15 dyne/cm^2) after 24 h ($n > 10$; data are mean ± SD). Statistical analyses: two-way ANOVA: interaction ($p < 0.001$).

(F) Change in cell counts per image of negative-control-siRNA- and CFTR-siRNA-treated HMVEC-Ls before and after SS for 24 h ($n = 14$; data are mean ± SD). Statistical analyses: two-tailed Student's t test.

(G) Representative images of live recording of HMVEC-Ls subjected to SS (15 dyne/cm^2) showing progressive cell retraction and formation of gaps in the endothelial monolayer (scale bar: 1,000 μm).

(H) Representative immunofluorescence images showing vascular endothelial cadherin (VE-cad) expression (green) of DMSO and CFTRinh-172-treated HMVEC-Ls in static or flow conditions (15 dyne/cm^2) after 24 h (scale bar: 100 μm). See also Figures S1–S4 and Videos S1 and S2. *$p \leq 0.05$; **$p \leq 0.01$; ***$p \leq 0.001$; ****$p \leq 0.0001$.

RESULTS

CFTR deficiency promotes barrier failure in lung microvascular endothelial cells in the presence of shear stress

Since CFTR is expressed and functional in ECs (Figure S1), and vascular perturbations and perfusion deficits are reported in CF patients,[2–6] we hypothesized that pulmonary vascular remodeling may occur in CF. In a pilot study, we performed pulmonary vascular morphometry and reconstructed the pulmonary vasculature of 40 individuals with CF. We found that early in the clinical course of CF when pulmonary function is normal, most of the total blood volume (TBV) is in small blood vessels (cross-sectional surface area [CSA] < 10 mm^2). However, in CF patients with severe lung disease, most of the TBV was in larger blood vessels (Figures 1A and S2). We suspected that this extensive remodeling was due to loss of SPBVs and progressive redistribution of total blood volume to larger vessels.

Hemodynamics varies between small and large blood vessels, especially SS, which plays a critical role in EC migration, proliferation, flow alignment, and NO production.[9–13] Depending on the severity of CF lung disease, patients may develop pulmonary hypertension,[29–31] which can result in higher pressure and increased SS.[32,33] Therefore, we decided to investigate the response of CFTR-defective (by knockdown or inhibition) HMVEC-Ls under high SS using a vessel-on-a-chip model (Figures 1B, 1C, and S3). We used SS of 15 dyne/cm^2, which is within the physiological range for healthy adults (10–25 dyne/cm^2).[15,28]

In static conditions (e.g., without SS), inhibiting CFTR with CFTR-specific inhibitor CFTRinh-172,[34] or knocking down CFTR, had no adverse effects on cell viability compared to control. However, applying SS to CFTR-defective ECs for 24 h caused significant apoptosis compared to control (Figures 1D–1F and S4).

Live recordings revealed that high SS causes a progressive retraction of ECs from one another and subsequent formation of gaps in the monolayer (Figure 1G and Videos S1 and S2). A recent CFTR study reported similar observations under low SS (5 dyne/cm^2).[6]

We speculated that the cell retraction was due to degradation of adherens junctions (AJs) and loss of cell-cell contact. Staining for vascular endothelial cadherin (VE-cad), the main component of AJs, revealed strong expression of VE-cad in static conditions in both control and CFTRinh-172-treated cells. However, under SS, inhibiting CFTR caused a significant reduction in VE-cad expression; this reduction was more pronounced in cells displaying a greater degree of retraction (Figure 1H). These findings suggest that loss of AJs leads to reduced cell viability when CFTR is defective under SS.

Overactivation of mechanosensitive channel TRPV4 causes shear-stress-dependent barrier failure when CFTR is defective

AJs have been shown to be directly cleaved by calcium-dependent ubiquitous protease calpains.[27,35–37] Only two calpain isoforms are expressed in ECs: μ-calpain and m-calpain.[38] μ-calpain requires only micromolar concentration of calcium for activation, whereas m-calpain requires almost three orders of magnitude more calcium.[39] Only m-calpain specifically can cleave AJs.[36,40] Therefore, we hypothesized that there must be a more robust SS-dependent intracellular calcium increase in ECs when CFTR is defective to chronically activate m-calpain.

Live calcium imaging revealed a low static baseline level of intracellular calcium that rose sharply in response to a 1-min SS stimulus (Videos S3 and S4).[41] The rise was more pronounced and sustained when *CFTR* was knocked down compared to control (Figures 2B–2D).

We inferred that this higher rise in calcium would lead to higher calpain activity. To measure the real-time activity of calpain in response to SS, we used CMAC-t-BOC-Leu-Met, a cell-permeable compound that is non-fluorescent in the extracellular environment. Once inside the cell, this compound is cleaved by activated calpain, becomes impermeable, and fluoresces (Figure 2E and Video S5).[42] We found higher calpain activity when *CFTR* was knocked down compared to control (Figures 2F and 2G), which can disrupt expression of AJs.[27] Next, we inhibited CFTR while also inhibiting calpain using the endogenous inhibitor calpastatin; this inhibitor binds calpain only after it is activated by calcium and has a higher affinity for m-calpain.[43] These steps mitigated the detrimental effects of CFTR deficiency under SS (Figures 2H and 2I) and suggest that calpain plays a role in the mechanism of barrier failure in CF.

To study the effects of chronic calcium entry on EC viability, we used calcium ionophore A23187 and found that high intracellular calcium levels led to cell death (Figure 2J and Video S6). Since the effects of CFTR deficiency were only noticeable in the presence of SS, we suspected an upstream involvement of MsCs. Two channels, PIEZO1 and TRPV4, stood out because they are not only directly activated by SS but also permeable to calcium.[27,44–50] Furthermore, PIEZO1 has been shown to act upstream of TRPV4 by activating phospholipase A2, which is required for the activation of TRPV4.[41]
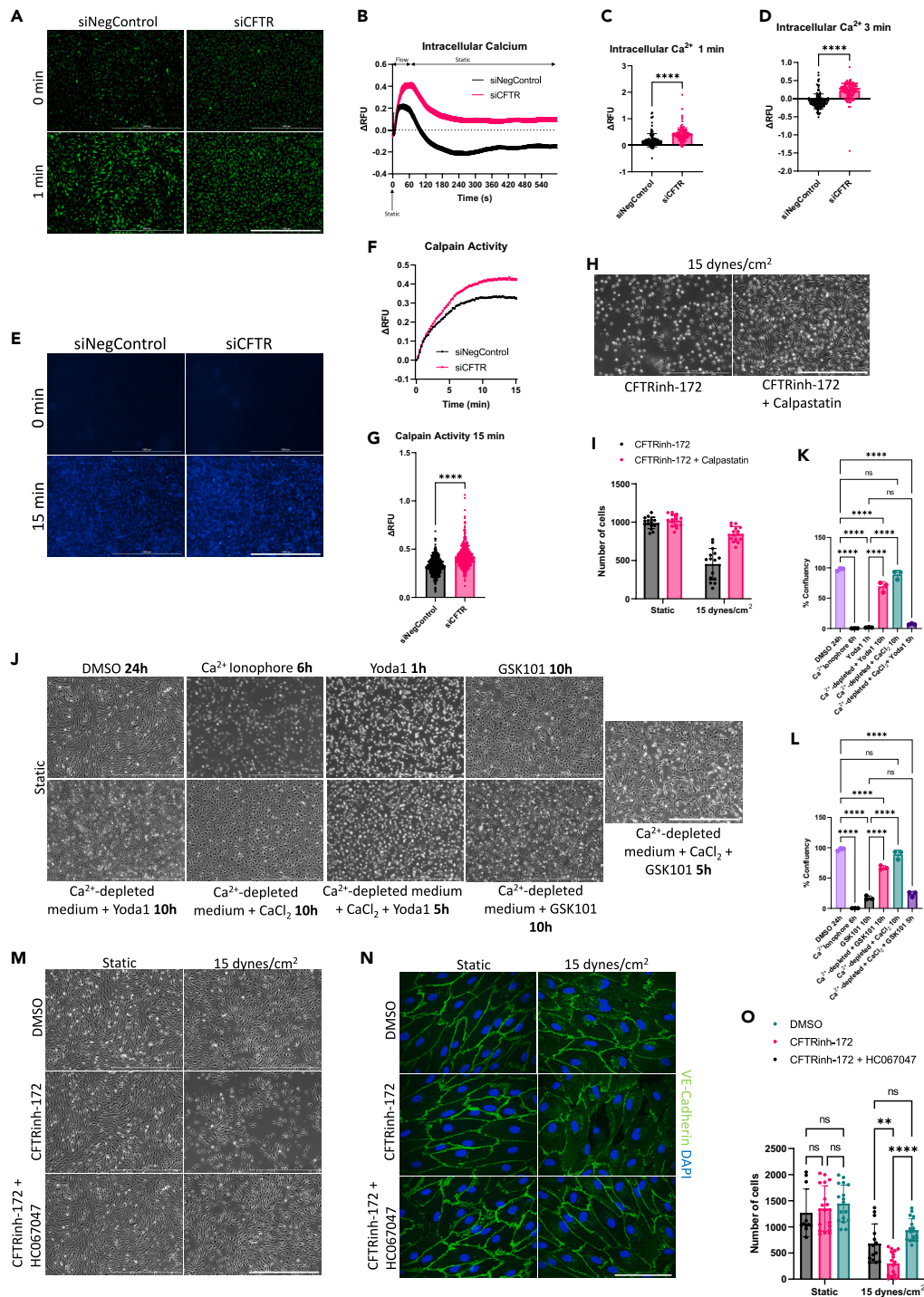
Figure 2. Overactivation of TRPV4 causes shear-stress-dependent loss of endothelial monolayer integrity when CFTR is defective

(A) Representative images of live recording of intracellular calcium levels (green fluorescence) of HMVEC-Ls under shear stress (SS) (15 dyne/cm^2) used to quantify data in (B), (C) and (D) (scale bar: 1,000 μm).

(B–D) (B) Time courses used to quantify data in (C) and (D). Change in intracellular calcium levels of negative-control-siRNA- and CFTR-siRNA-treated HMVEC-Ls subjected to SS (15 dyne/cm^2) for only 1 min out of the 10-min total recording time (*n* = 131 cells; data are mean ± SE). (C and D) Change in intracellular calcium levels from (B) at 1 min (C) and at 3 min (D) (*n* = 131 cells; data are mean ± SD). Statistical analyses: two-tailed Student's t test.

(E) Representative images of live recording of intracellular calpain activity (blue fluorescence) of HMVEC-Ls under SS (15 dyne/cm^2) used to quantify data in (F) and (G) (scale bar: 1,000 μm).

Figure 2. Continued

(F) Representative time courses used to quantify data in (G). Change in intracellular calpain activity of negative-control-siRNA- and CFTR-siRNA-treated HMVEC-Ls subjected to SS (15 dyne/cm^2) for 15 min (n = 431 cells; data are mean $\pm$ SE).

(G) Change in intracellular calpain activity from (F) at 15 min (n = 431 cells; data are mean $\pm$ SD). Statistical analyses: two-tailed Student's t test.

(H) Representative images used to quantify data in (I) of HMVEC-Ls subjected to SS (15 dyne/cm^2) for at least 24 h (scale bar: 1,000 μm). HMVEC-Ls were treated with 20 μM CFTRinh-172 only, or with a combination of 20 μM CFTRinh-172 and 500 nM calpastatin.

(I) Cell counts per image of CFTRinh-172- and CFTRinh-172 + calpastatin-treated HMVEC-Ls in static or flow conditions (15 dyne/cm^2) after 24 h (n = 15; data are mean $\pm$ SD). Statistical analyses: two-way ANOVA: interaction (p < 0.0001).

(J) Representative images used to quantify data in (K) and (L) (scale bar: 1,000 μm). HMVEC-Ls were treated with DMSO, 3 μM calcium ionophore A23187, 2.5 μM Yoda1, and 50 μM GSK1016790A, in regular medium, calcium-depleted medium, or calcium-depleted medium supplemented with 50 mM CaCl$_2$. For all treatments, cells remained in static conditions.

(K and L) Percent cell confluency per image from (J) of DMSO-, calcium ionophore A23187-, Yoda1- (L), and GSK1016790A (K)-treated HMVEC-Ls in regular medium, calcium-depleted medium, or calcium-depleted medium supplemented with CaCl$_2$, in static conditions (n = 3; data are mean $\pm$ SD). Statistical analyses: one-way ANOVA with Tukey's multiple comparison.

(M) Representative images before immunofluorescence in (M) and used to quantify data in (N) (scale bar: 1,000 μm). HMVEC-Ls were treated with DMSO, 20 μM CFTRinh-172 only, or with a combination of 20 μM CFTRinh-172 and 1 μM TRPV4-specific inhibitor HC067047. For each treatment, cells either remained in static conditions or were subjected to SS (15 dyne/cm^2) for at least 24 h.

(N) Representative immunofluorescence images from (L) showing VE-cad expression (green) (scale bar: 100 μm).

(O) Cell counts per image of DMSO-, CFTRinh-172-, and CFTRinh-172 + HC067047-treated HMVEC-Ls in static or flow conditions (15 dyne/cm^2) after 24 h (n > 10; data are mean $\pm$ SD). Statistical analyses: two-way ANOVA with Tukey's multiple comparison: interaction (p < 0.01). See also Videos S3, S4, S5, S6, S7, and S8.

*$p \leq 0.05$; **$p \leq 0.01$; ***$p \leq 0.001$; ****$p \leq 0.0001$.

We started by investigating if chronic activation of PIEZO1 by selective agonist Yoda1[51] would also lead to cell death. We found that chronic activation of PIEZO1 led to rapid cell death (about 1 h); this occurred only in the presence of calcium (Figures 2J and 2K and Video S7). Therefore, we rationalized that chronic activation of PIEZO1 in response to SS might be leading to cell death when CFTR is defective. We inhibited PIEZO1 using a cationic-permeable MsCs inhibitor GsMTx-4 while also inhibiting CFTR under SS[52]; these steps were not sufficient to rescue the cells (Figures S5A and S5B). It should be noted that GsMTx-4, though non-specific for PIEZO1, does not inhibit TRPV4.[41]

Interestingly, although PIEZO1 activation reportedly leads to a transient intracellular calcium elevation, TRPV4 activation induces a stronger and more sustained rise.[41] Therefore, TRPV4 is better equipped to provide the required calcium levels to activate m-calpain. Besides, calcium entry via TRPV4 specifically increases lung endothelial permeability; when calcium enters ECs via another calcium channel, α_{1G}, endothelial permeability is not altered.[53] We reasoned that this difference could be explained by the propensity of TRPV4 to induce stronger intracellular calcium elevation. Additionally, calcium entry via TRPV4 has previously led to the remodeling of AJs in ECs.[54] Evidence from animal models also highlights the relevance of TRPV4; when TRPV4 is activated by a specific agonist, GSK1016790A (GSK101), pulmonary edema and alveolar hemorrhage occur in the lungs of rats.[55–57] For all these reasons, further investigation of TRPV4 was warranted.

Chronic activation of TRPV4 by GSK101[56,57] led to progressive cell retraction and formation of intercellular gaps in the endothelial monolayer (about 10 h); these changes occurred only in the presence of calcium (Figures 2J and 2L and Video S8). Next, we inhibited TRPV4 using a TRPV4-specific inhibitor, HC067047,[58] while also inhibiting CFTR under SS; similar to the inhibition of calpain, the inhibition of TRPV4 was sufficient to rescue the cells and maintain the integrity of AJs (Figures 2M–2O). These results are comparable to those from a study demonstrating that endothelial activity of PAR1, a TRPV4 sensitizer, leads to sustained calcium elevation and increased vascular permeability through disruption of AJs. Moreover, TRPV4 inhibition mitigated the detrimental effects of PAR1 activation.[59] A recent *in vivo/ex vivo* study in the lungs of rats and mice also showed that CFTR deficiency leads to increased endothelial calcium response, loss of endothelial barrier integrity, and edema formation. TRPV4 inhibition or knockdown (KD) prevented these effects.[60] Taken together, these studies suggest that proteins and molecules that lower the activation threshold of TRPV4 could lead to calcium overload and increased vascular permeability. Thus, we rationalized that CFTR could modulate TRPV4 function.

CFTR deficiency alters lipid metabolism and cytoskeleton organization

Proteins and molecules that change the fluidity or curvature of the membrane have been found to modulate MsCs.[61,62] In fact, a stiffer membrane inhibits MsCs, whereas a more fluid membrane enhances their activation.[63–65] Because the membrane is made up of lipids, changes in lipid composition can directly affect membrane mechanical properties, including fluidity.[66,67]

Defective CFTR expression has been shown to increase sphingolipid synthesis and change membrane composition.[68] Moreover, sphingosine-1-phosphate (S1P), a signaling sphingolipid known to increase AJs' expression and barrier impermeability, may be transported by CFTR.[69–72] In fact, S1P supplementation mitigated loss of endothelial barrier integrity when CFTR was inhibited or knocked down.[73] Taken together, these findings suggest CFTR plays a role in lipid regulation.

We performed bulk RNA sequencing on control and CFTR-KD HMVEC-Ls to investigate lipid metabolism. For technical reasons, RNA sequencing was performed on cells cultured in static conditions. Nonetheless, this approach allows us to appreciate gene expression changes caused by *CFTR* KD without the confounding factor of flow. We found 349 genes to be differentially expressed in CFTR-KD HMVEC-Ls. The top 30 differentially expressed genes are plotted (Figure 3A), and the heatmap shows a consistent signature across samples (Figure 3B).

Ingenuity pathway analysis revealed changes in vascular system and lipid synthesis. For example, there was a significant upregulation of vascular permeability, an overall upregulation of angiogenesis/vasculogenesis (possibly as a compensatory mechanism), and an overall
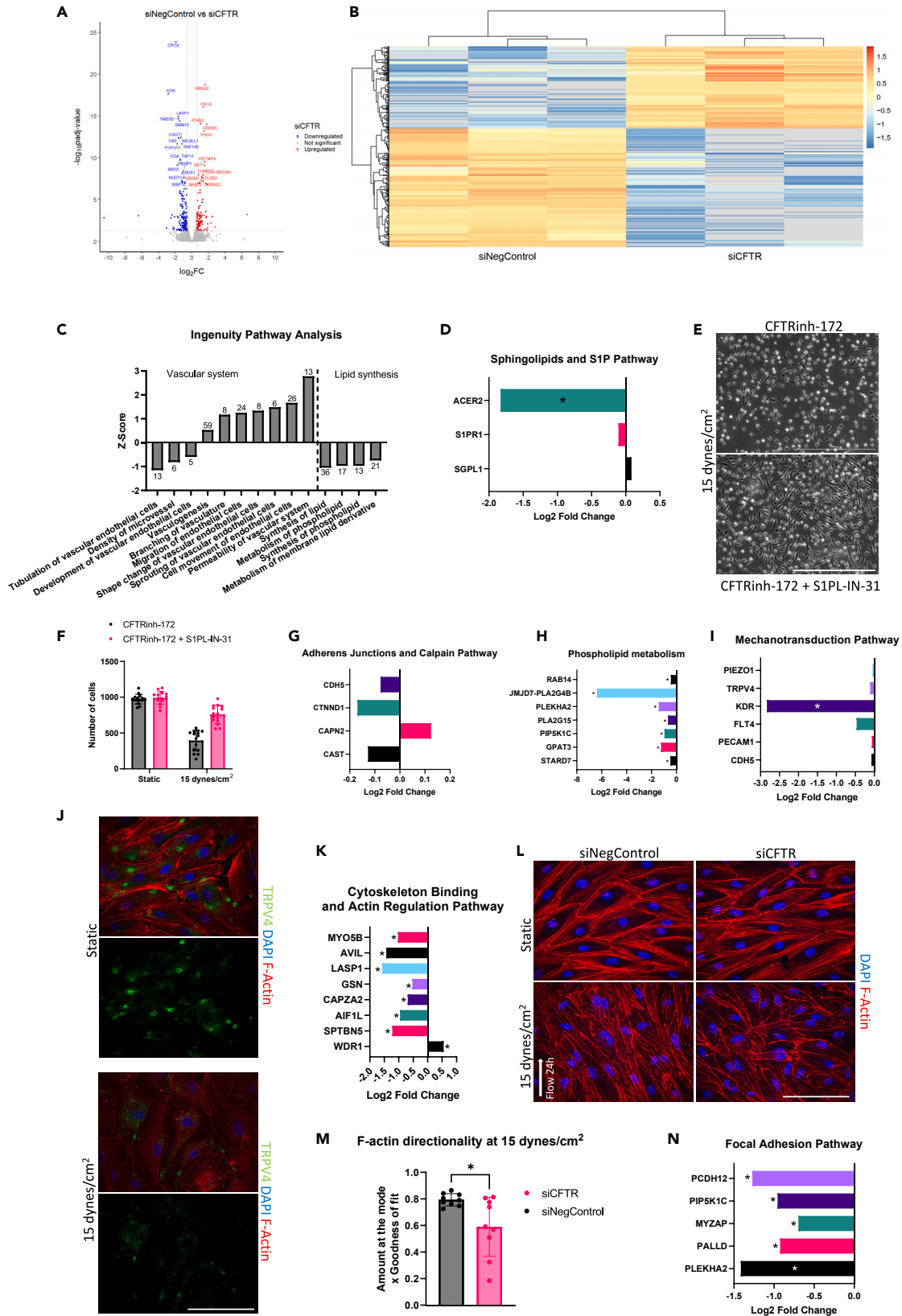
A siNegControl vs siCFTR

B

C Ingenuity Pathway Analysis

D Sphingolipids and S1P Pathway

E CFTRinh-172 / CFTRinh-172 + S1PL-IN-31

F CFTRinh-172 / CFTRinh-172 + S1PL-IN-31

G Adherens Junctions and Calpain Pathway

H Phospholipid metabolism

I Mechanotransduction Pathway

J Static / 15 dynes/cm² — TRPV4 DAPI F-Actin

K Cytoskeleton Binding and Actin Regulation Pathway

L siNegControl / siCFTR — Static / 15 dynes/cm² — DAPI F-Actin

M F-actin directionality at 15 dynes/cm²

N Focal Adhesion Pathway

Figure 3. CFTR knockdown leads to lipid metabolic changes and cytoskeleton reorganization

(A) Volcano plot of differentially expressed genes (DEGs) in CFTR-siRNA-treated HMVEC-Ls compared to control. Names of top 30 genes are displayed.

(B) Heatmap of DEGs in negative-control-siRNA- and CFTR-siRNA-treated HMVEC-Ls.

(C) Differentially regulated pathways of CFTR-siRNA-treated HMVEC-Ls predicted by ingenuity pathway analysis with Z score of at least ± 0.5. Numbers of DEGs are indicated on bars.

(D) Change in gene expression of select genes involved in sphingolipids and S1P metabolism in CFTR-siRNA-treated HMVEC-Ls compared to control. *DEG.

(E) Representative images used to quantify data in (F) of HMVEC-Ls subjected to SS (15 dyne/cm^2) for at least 24 h (scale bar: 1,000 μm). HMVEC-Ls were treated with 20 μM CFTRinh-172 only or with a combination of 20 μM CFTRinh-172 and 1 μM S1PL-IN-31.

(F) Cell counts per image of CFTRinh-172- and CFTRinh-172 + S1PL-IN-31-treated HMVEC-Ls in static or flow conditions (15 dyne/cm^2) after 24 h (n = 15; data are mean $\pm$ SD). Statistical analyses: two-way ANOVA: interaction ($p < 0.0001$).

(G–I) Change in gene expression of select genes involved in adherens junctions and calpain activity regulations (G), phospholipid metabolism (H), and mechanotransduction (I) in CFTR-siRNA-treated HMVEC-Ls compared to control. *DEG.

(J) Representative immunofluorescence images showing TRPV4 surface expression (green) and F-actin expression (red) of HMVEC-Ls in static or flow conditions (15 dyne/cm^2) after 24 h (scale bar: 100 μm).

(K) Change in gene expression of select genes involved in cytoskeleton binding and actin regulation in CFTR-siRNA-treated HMVEC-Ls compared to control. *DEG.

(L) Representative immunofluorescence images used to quantify data in (M) (scale bar, 100 μm). F-actin staining (red) of negative-control-siRNA- and CFTR-siRNA-treated HMVEC-Ls in static or flow conditions (15 dyne/cm^2) after 24 h. White arrow depicts direction of flow.

(M) Modal amount and goodness of fit of actin filaments with direction of flow for negative-control-siRNA- and CFTR-siRNA-treated HMVEC-Ls. Directionality analysis of F-actin filaments was performed using directionality tool in Fiji (ImageJ) with local gradient orientation method. Statistical analyses: two-tailed Student's t test.

(N) Change in gene expression of select genes involved in focal adhesion in CFTR-siRNA-treated HMVEC-Ls compared to control. *DEG. See also Figure S6 and Videos S9 and S10. *$p \leq 0.05$; **$p \leq 0.01$; ***$p \leq 0.001$; ****$p \leq 0.0001$.

downregulation of lipid synthesis (Figure 3C). Using the DAVID database, we identified several genes enriched in pathways of interest. We decided to focus not only on genes that were significantly differentially expressed but also on the trends of certain important genes (e.g., upregulation or downregulation, though not significant).

Selected genes in the sphingolipids and S1P pathway show that *ACER2*, a ceramidase responsible for the hydrolysis of ceramides into sphingosine, the precursor of S1P, is significantly downregulated. Expression of *SGPL1*, the gene that encodes S1P lyase (the enzyme responsible for breakdown of S1P), tends to be upregulated. Additionally, the expression of *S1PR1* (the gene that encodes S1P receptor 1) tends to be downregulated (Figure 3D). All of this points to downregulation of S1P signaling. We found that raising intracellular S1P levels by inhibiting S1P lyase activity with S1PL-IN-31 was sufficient to mitigate the detrimental effects of CFTR deficiency under SS (Figures 3E and 3F). As mentioned earlier, S1P increases AJs surface expression.[69,71] Therefore, these results indicate that AJs disassembly is pivotal to the loss of endothelial barrier integrity when CFTR is defective under SS. Thus, we also looked at the AJs pathway and found that expression of *CDH5* (VE-cad), and of its membrane regulator *CTNND1* (p120-catenin),[74] tend to be downregulated. Furthermore, the expression of *CAPN2* (m-calpain) tends to be upregulated, whereas the expression of *CAST* (calpastatin), the endogenous inhibitor of calpain, tends to be downregulated (Figure 3G).

We also found an overall downregulation of genes associated with phospholipid synthesis (Figure 3H), which could change membrane composition and dynamics and affect mechanotransduction. We investigated the two main endothelial MsCs and found that neither *PIEZO1* nor *TRPV4* expression levels were changed (Figure 3I). However, *KDR* (vascular endothelial growth factor receptor 2 [VEGFR2]) expression level was drastically reduced (Figure 3I). This reduction is significant because VEGFR2 forms a junctional sensory complex with VEGFR3 (*FLT4*), CD31 (*PECAM1*), and VE-cad (*CDH5*) that mediates SS signaling.[75,76] We speculate that reduced VEGFR2 expression and loss of VE-cad are likely to alter mechanosensation when CFTR is defective. Besides, the signaling cascade that occurs when VEGF, which is significantly increased in the serum of CF patients, binds to VEGFR2 is critical for EC proliferation, migration, survival, and angiogenesis.[77,78] A notable disruption in VEGF/VEGFR2 signaling could prevent new blood vessel formation (Figure S6 and Videos S9 and S10), wound healing, and further exacerbate loss of SPBVs. However, it is important to note that even though angiogenesis appears to be reduced in the CF pulmonary microvasculature, there are several reports of the opposite in larger vessels such as the bronchial vessels.[79,80] In fact, the bronchial circulation, thanks to its higher proliferative capacity, undergoes increased angiogenesis in CF.[79–82] This phenomenon is also observed in other inflammatory diseases such as asthma and interstitial pulmonary fibrosis.[81,82] Though beneficial in the short term by increasing gas exchange, this increased vascularization poses the risk of massive hemoptysis (blood vessel rupture, coughing up blood).[79,81,82] The reason for the difference in angiogenic activity between capillaries and larger vessels is unclear. Nonetheless, we believe it could be due to a difference in SS and VEGF/VEGFR2 signaling.

Additionally, since (1) the effect of CFTR deficiency is only apparent under SS and (2) transcriptomics data show that *TRPV4* expression is unaltered when CFTR is defective, we hypothesized that there must be an SS-dependent regulation of TRPV4 surface expression. Consequently, we performed immunofluorescence staining using an anti-TRPV4 antibody that binds to an extracellular loop of TRPV4. This staining was performed without permeabilization to ensure binding only to TRPV4 on the cell surface. Also, F-actin staining helped highlight the overall structure of the cell. We found that in static conditions, TRPV4 was mainly expressed in clusters at intercellular junctions. However, clustering was abrogated under SS (Figure 3J). A recent study showed that under static conditions, TRPV4 channels cluster and form a complex with β-catenin at the AJs. SS leads to reduced clustering of TRPV4, its dissociation from β-catenin, and its translocation to the basal
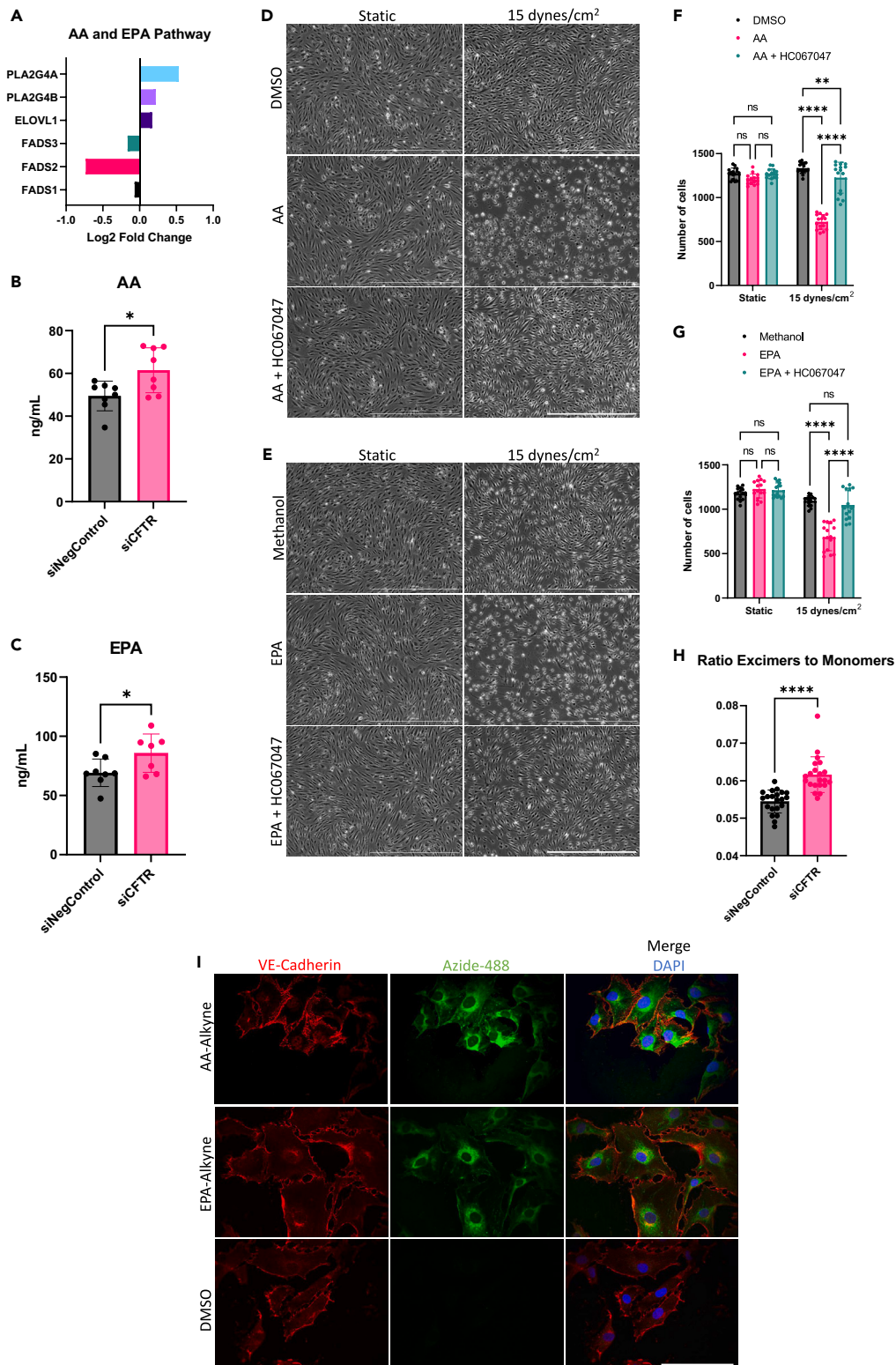
Figure 4. CFTR deficiency lowers the flow-induced activation threshold of TRPV4 through changes in AA and EPA metabolism and increased membrane fluidity

(A) Change in gene expression of select genes involved in AA and EPA metabolism in CFTR-siRNA-treated HMVEC-Ls compared to control. *DEG.

Figure 4. Continued

(B and C) AA (B) and EPA (C) content analyzed by liquid chromatography-tandem mass spectrometry in negative-control-siRNA- and CFTR-siRNA-treated HMVEC-Ls. Statistical analyses: two-tailed Student's t test.

(D and E) Representative images used to quantify data in (F) and (G) (scale bar: 1,000 μm). HMVEC-Ls were pre-treated for 24 h with DMSO (D) or methanol (E), 20 μM AA (D) or 40–80 μM EPA[100] (E), or with a combination of 20 μM AA (D) or 40–80 μM EPA (E), and 1 μM TRPV4-specific inhibitor HC067047. For each treatment, cells either remained in static conditions or were subjected to SS (15 dyne/cm^2) for at least an additional 24 h.

(F and G) Cell counts per image of DMSO (F) or methanol (G), AA (F) or EPA (G), and AA (F) or EPA (G) + HC067047 24 h pre-treated HMVEC-Ls in static or flow conditions after an additional 24 h ($n > 10$; data are mean ± SD). Statistical analyses: two-way ANOVA with Tukey's multiple comparison: interaction (F) and (G) ($p < 0.0001$).

(H) Excimers to monomers ratio of pyrenedecanoic acid (PDA) in the membrane of negative-control-siRNA- and CFTR-siRNA-treated HMVEC-Ls. The greater the ratio of excimers to monomers, the more fluid the membrane.

(I) Representative immunofluorescence images showing membrane expression of VE-cad (red) and AA-alkyne or EPA-alkyne clicked with azide-488 (green) (scale bar: 100 μm). HMVEC-Ls were treated with DMSO, 20 μM AA-alkyne, or 20 μM EPA-alkyne for 48 h. *$p \leq 0.05$; **$p \leq 0.01$; ***$p \leq 0.001$; ****$p \leq 0.0001$.

membrane.[83] Thus, we proposed that TRPV4, when in a complex with β-catenin, might stabilize AJs. This protective effect is lost when TRPV4 is translocated to the basal membrane. Consequently, when CFTR is defective and SS is applied, the instability of β-catenin, combined with the cleavage of VE-cad, could result in faster degradation of AJs.

Also, the loss of mechanotransduction has further implications. Impaired mechanotransduction has been associated with reduced EC alignment and actin cytoskeleton disorganization.[76,84–86] Several genes in the cytoskeleton binding and actin regulation pathway, such as *MYO5B* and *LASP1*, are significantly downregulated when *CFTR* is knocked down (Figure 3K). Interestingly, *MYO5B*, an actin-based mechanoenzyme, appears to be required for trafficking of CFTR to the plasma membrane and to recycling endosomes.[87] Moreover, gene expression of *WDR1*, an actin-regulating protein that induces actin filament disassembly, is increased.[88,89]

Since SS induces EC cytoskeleton remodeling and alignment in the direction of flow,[84–86] we hypothesized that F-actin organization under SS would be disrupted when *CFTR* was knocked down. We found similar F-actin protein expression for control and CFTR-KD ECs in static conditions. However, F-actin expression was reduced and completely disorganized under SS in CFTR-KD ECs (Figures 3L and 3M).

Given the direct role of actin in the regulation of focal adhesion molecules,[90–92] we sought to determine if the focal adhesion pathway was affected. We discovered that several key genes were downregulated (Figure 3N). These findings suggest that CFTR-defective ECs are less likely to stay anchored to the extracellular matrix under SS, which further aggravates loss of barrier integrity.

CFTR deficiency sensitizes TRPV4 to fluid SS through changes in AA and EPA metabolism and increased membrane fluidity

Besides phospholipid and sphingolipid imbalances, polyunsaturated fatty acid (PUFA) imbalances have also been identified in CF patients and CFTR-knockout mice. Specifically, an increase in arachidonic acid (AA) and a decrease in docosahexaenoic acid (DHA) levels have been noted.[93,94] These imbalances were also reported in nasal epithelial cells of CF patients, regardless of pancreatic sufficiency.[95,96] Also, expression of defective CFTR led to increased eicosapentaenoic acid (EPA) levels in human bronchial epithelial cells.[97–99]

In the membrane, AA and EPA are typically part of the acyl chains of phospholipids. However, they can also occur as free fatty acids derived from the hydrolysis of phospholipids by phospholipases.[66] When incorporated into the lipid bilayer, AA and EPA can alter the mechanical properties of the cell membrane and modulate the activity of MsCs.[63,64,66]

Our transcriptomic analysis revealed that expression of *FADS2*, the enzyme that catalyzes the first and rate-limiting step in the synthesis of AA and EPA from essential fatty acid precursors linoleic acid (LA) and alpha linoleic acid (αLA), tends to be downregulated (Figure 4A). LA and αLA levels are reported to be reduced in the serum of CF patients,[99] which correlates with the lower enzymatic activity of FADS2. Nonetheless, *PLA2G4A* and *PLA2G4B*, the genes that encode cytosolic phospholipase A2 (the enzyme that catalyzes the release of AA from phospholipids), tend to be upregulated (Figure 4A). *ELOVL1*, a gene that enables elongase activity, which is crucial in AA, EPA, and sphingolipid syntheses, also tends to be upregulated (Figure 4A). Therefore, based on these results and the aforementioned studies suggesting an association between CF deficiency and increased AA and EPA levels, we rationalized that CFTR-defective HMVEC-Ls would also display increased AA and EPA levels. We quantified free AA and EPA levels using targeted liquid chromatography-tandem mass spectrometry; we discovered that CFTR-KD HMVEC-Ls had significantly higher AA and EPA levels than control cells (Figures 4B and 4C).

This increase in AA and EPA when CFTR is defective is critical because AA, EPA, and their respective metabolites, 5′6′-EET and 17′18′-EEQ, have been shown to dramatically lower the activation threshold of TRPV4 or directly bind to and activate it.[64,101–103] To confirm that AA and EPA can directly upregulate the activity of TRPV4 in HMVECs-L, we supplemented cell culture medium with AA or EPA while inhibiting TRPV4 with HC067047. We found that under static conditions, supplementing AA or EPA had no adverse effects on cell viability compared to control (Figures 4D–4G). However, under SS, there was a drastic reduction in cell viability compared to control when AA and EPA were supplemented, much like what occurs in CFTR deficiency. These negative effects were also prevented by TRPV4 inhibition (Figures 4D–4G). Overall, results indicate that AA and EPA significantly lower the mechanical stress activation threshold of TRPV4.

Changes in PUFAs levels can impact the architecture of the membrane. In fact, PUFAs have been reported to increase membrane structural disorder and fluidity.[104,105] Because MsCs are gated by bilayer tension, increased fluidity results in enhanced TRPV4 activation.[63–65] We performed fluorescence anisotropy and found a significant increase in EC membrane fluidity when *CFTR* was knocked down compared to control (Figure 4H).
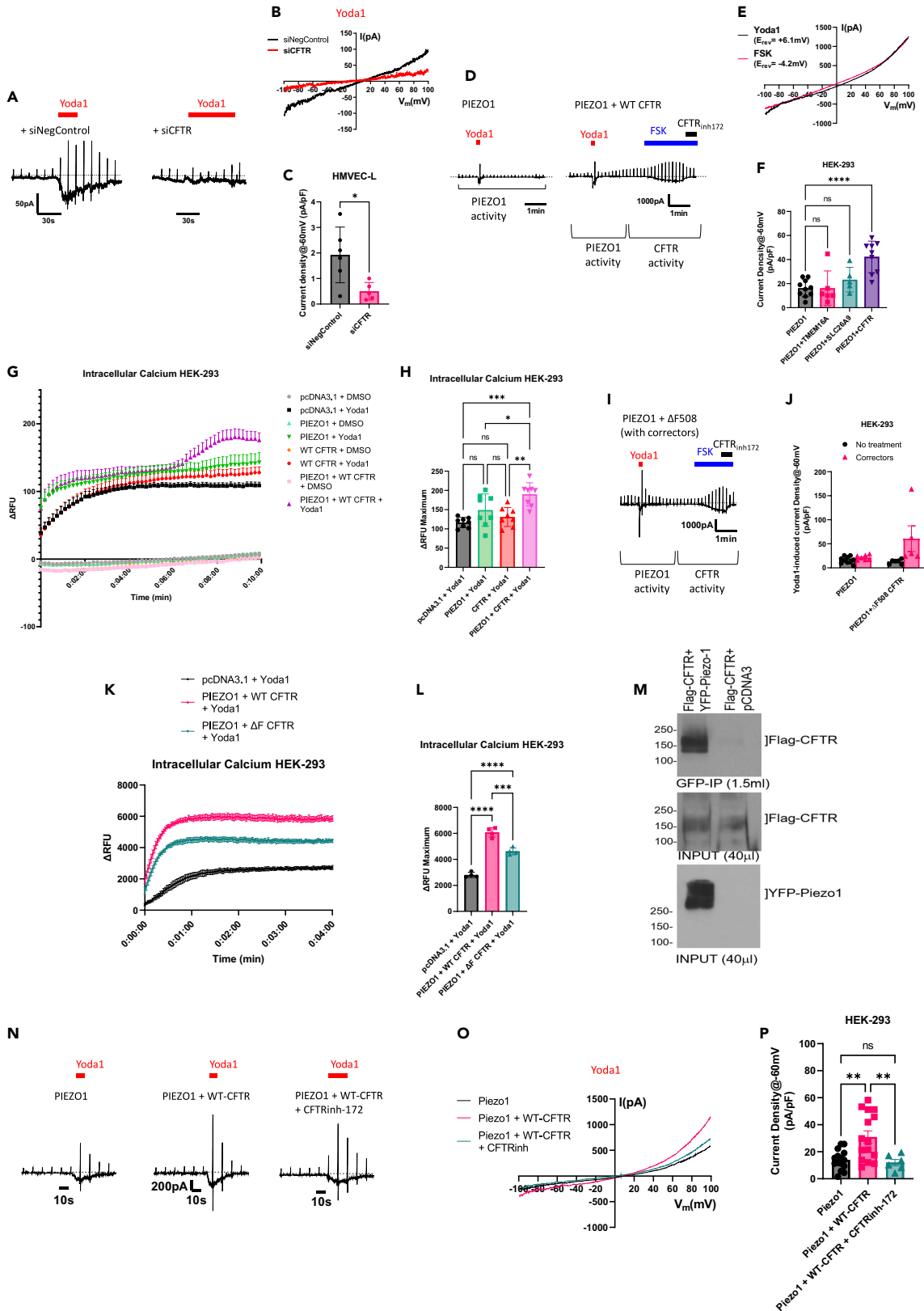
Figure 5. CFTR directly interacts with PIEZO1 and enhances its function

(A) Representative traces of whole-cell currents of negative-control-siRNA- and CFTR-siRNA-treated HMVEC-Ls. Bath solution contained 10 μM Yoda1.

(B) Representative I–V curves from (A).

(C) Summary of Yoda1-induced current in negative-control-siRNA- and CFTR-siRNA-treated HMVEC-Ls ($n > 5$; data are mean ± SD). Statistical analyses: two-tailed Student's t test.

(D) Representative traces of whole-cell currents of HEK-293 cells transfected with PIEZO1 only, or cotransfected with PIEZO1 and WT CFTR. Bath solution contained 10 μM Yoda1, 20 μM Forskolin, and 20 μM CFTRinh-172.

(E) Representative I–V curves from (D).

(F) Summary of Yoda1-induced current in HEK-293 cells transfected with PIEZO1 only, or cotransfected with PIEZO1 and TMEM16A, or with PIEZO1 and SLC26A9, or with PIEZO1 and CFTR ($n > 5$; data are mean ± SD). Statistical analyses: one-way ANOVA with Dunnett's multiple comparison.

(G) Time courses used to quantify data in (H). DMSO or 25 μM Yoda1-induced change in intracellular calcium levels of HEK-293 cells transfected with empty vector only, PIEZO1 only, CFTR only, or cotransfected with PIEZO1 and CFTR ($n = 8$ wells; data are mean ± SE).

(H and G) Change in intracellular calcium levels from (G) using maximum fluorescence intensity ($n = 8$ wells; data are mean ± SD). Statistical analyses: one-way ANOVA with Tukey's multiple comparison.

(I) Representative traces of whole-cell currents of HEK-293 cells cotransfected with PIEZO1 and CFTR mutant F508del, pre-treated with combination of CFTR correctors VX445/VX661 (2 μM each) for 24 h.[107] Bath solution contained 10 μM Yoda1, 20 μM Forskolin, and 20 μM CFTRinh-172.

(J) Summary of Yoda1-induced current in HEK-293 cells transfected with PIEZO1 only or cotransfected with PIEZO1 and CFTR mutant F508del. Cells were pre-treated with or without combination of CFTR correctors VX445/VX661 (2 μM each) for 24 h ($n > 5$; data are mean ± SD). Statistical analyses: two-way ANOVA: interaction ($p < 0.05$).

(K) Representative time courses used to quantify data in (L). 100 μM Yoda1-induced change in intracellular calcium levels of HEK-293 cells transfected with empty vector only, or cotransfected with PIEZO1 and WT CFTR, or with PIEZO1 and F508del CFTR ($n = 4$ wells; data are mean ± SE).

(L) Change in intracellular calcium levels from (K) using maximum fluorescence intensity ($n = 4$ wells; data are mean ± SD). Statistical analyses: one-way ANOVA with Tukey's multiple comparison.

(M) Coimmunoprecipitation blot of HEK 293 cells transfected with Flag-WT-CFTR only or co-transfected with Flag-WT-CFTR and PIEZO1-sYFP2.

(N) Representative traces of whole-cell currents of HEK-293 cells transfected with PIEZO1 only, or co-transfected with PIEZO1 and WT CFTR, and treated with or without 20 μM CFTRinh-172 in bath solution that also contained 10 μM Yoda1.

(O) Representative I–V curves from (N).

(P) Summary of Yoda1-induced current in HEK-293 transfected with PIEZO1 only, or co-transfected with PIEZO1 and WT CFTR, and treated with or without 20 μM CFTRinh-172 in bath solution ($n > 6$; data are mean ± SD). Statistical analyses: one-way ANOVA with Tukey's multiple comparison. *$p \leq 0.05$; **$p \leq 0.01$; ***$p \leq 0.001$; ****$p \leq 0.0001$.

To confirm that AA and EPA were indeed incorporated into the cell membrane where they could enhance TRPV4 activity, we performed click-chemistry-based immunofluorescence. We supplemented the culture medium of HMVEC-Ls with DMSO, AA-alkyne, or EPA-alkyne. We then clicked the cells with azide-488 while also costaining for VE-cad as a membrane indicator. We found that ECs were in fact incorporating supplemented AA and EPA into the membrane (Figure 4I). These results may be clinically relevant since AA is reportedly increased in the blood of CF patients.[94] CF ECs could be not only metabolizing more AA and EPA by themselves (Figures 4B and 4C) but also incorporating AA and EPA from the bloodstream directly into membrane-bound phospholipids; this could lead to further elevation of intracellular AA and EPA levels and potentially drive overactivation of TRPV4.

CFTR expression enhances PIEZO1 function

Ideally, loss of SPBVs should be mitigated by angiogenesis and wound repair. However, in CF pulmonary disease, TBV is redistributed to larger blood vessels, which suggests lack of angiogenesis (Figure 1A). Angiogenic sprouting is regulated by binding of VEGF to VEGFR2.[77] Impaired angiogenesis in CF could be due to the significant reduction in VEGFR2 expression (Figures 3I and S6), despite reports of elevated serum VEFG levels in CF patients.[78] However, PIEZO1 also regulates EC pathfinding in sprouting vessels during angiogenesis.[106] In fact, PIEZO1 has been shown to be critical for ECs SS sensing, migration, flow alignment, vasculogenesis, angiogenesis, wound repair, and apoptosis[25–27,106]—all of these functions are important in maintaining vascular integrity. We therefore hypothesized that CFTR deficiency might negatively regulate the activity of PIEZO1.

Whole-cell patch-clamping revealed that PIEZO1 activity was attenuated upon activation by specific agonist Yoda1 in CFTR-KD HMVEC-Ls when compared to control (Figures 5A–5C). To understand if PIEZO1 function could be dependent on CFTR expression, we transfected PIEZO1 by itself or cotransfected it with CFTR in HEK293 cells. We found that CFTR expression greatly enhanced PIEZO1 function (Figures 5D–5F). Because PIEZO1 is a cationic channel, we questioned whether the enhancing effect may occur because CFTR is a chloride channel. Therefore, we cotransfected PIEZO1 with other chloride channels/transporters such as TMEM16A and SLC26A9 and found that only CFTR had an enhancing effect on PIEZO1 function (Figure 5F). We then performed calcium imaging and found that Yoda1 induced a greater intracellular calcium increase in HEK-293 cells cotransfected with PIEZO1 and CFTR compared to cells transfected with PIEZO1 alone (Figures 5G and 5H).

Next, we coexpressed PIEZO1 with CFTR mutant F508del (folding mutation) in HEK-293 cells to investigate if the enhancement effect of CFTR was conformation dependent. On its own, expression of this variant did not enhance PIEZO1 function (Figure 5J). However, when treated with a combination of potent CFTR correctors (VX445 and VX661),[107] the corrected F508del mutant was able to enhance PIEZO1 function (Figures 5I and 5J). These results suggest that expression of WT-like CFTR is required to enhance PIEZO1 function. Furthermore, calcium
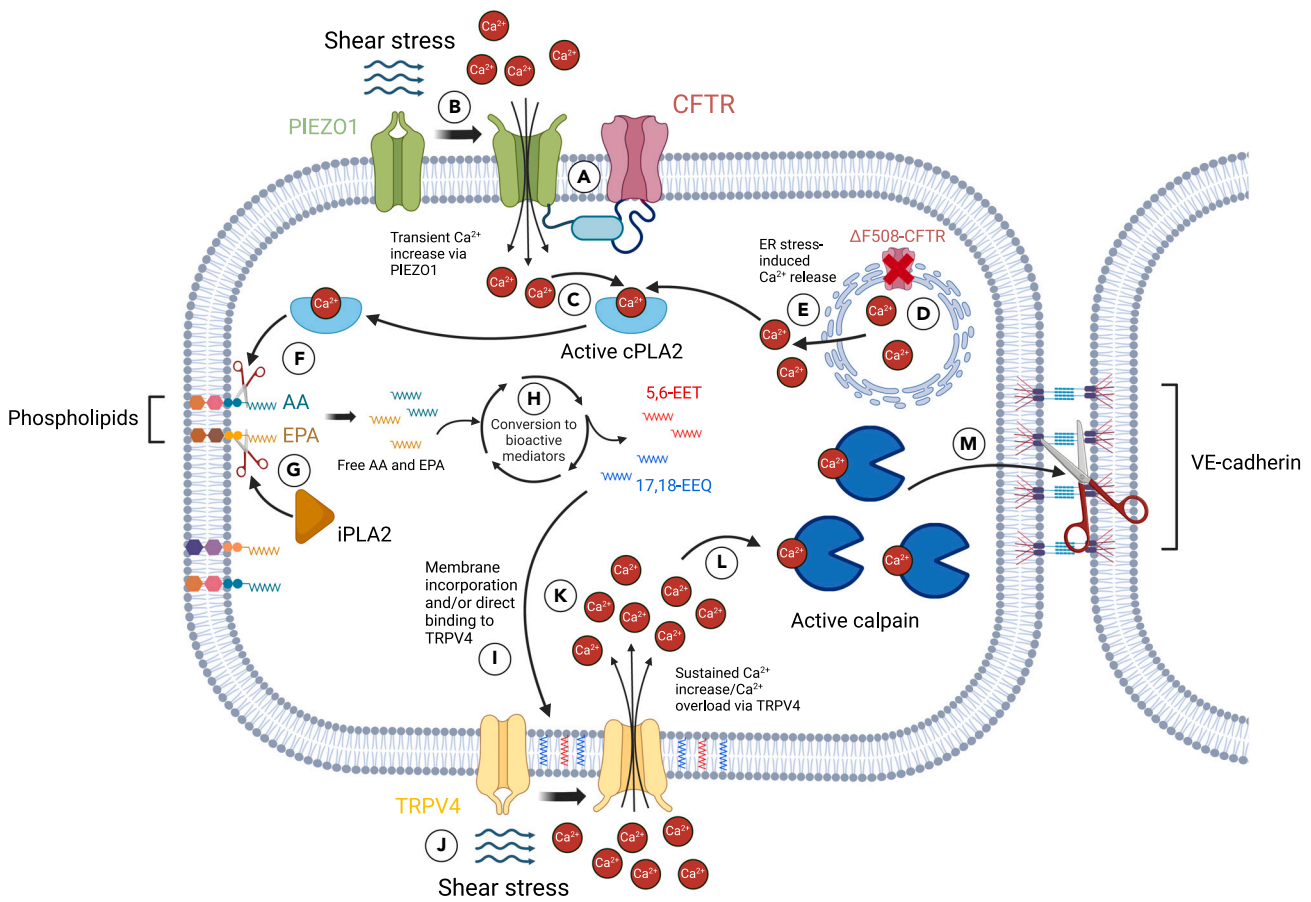
Figure 6. Proposed model of loss of endothelial barrier integrity

(A–C) In the *healthy endothelium*, functional CFTR and PIEZO1 directly interact at the cell membrane via unknown domains.

(D–M) In the case of *CF disease*, mutant CFTR, such as F508del-CFTR, is degraded in the ER, which limits interaction with PIEZO1. However, higher membrane content in AA, EPA, and their respective metabolites 5'6'-EET and 17'18'-EEQ[68,70,93,95–99] would lower the activation threshold of or even directly activate TRPV4.[63,64,101,102,105] This would lead to calcium overload and to overactivation of calcium-dependent m-calpain, which would result in faster degradation of VE-cad.[27,35–37,40]

imaging indicated that Yoda1 induces a greater intracellular calcium increase in HEK-293 cells cotransfected with PIEZO1 and WT CFTR compared to cells transfected with PIEZO1 and F508del CFTR mutant (Figures 5K and 5L). Therefore, we inferred that CFTR could directly interact with PIEZO1. We performed coimmunoprecipitation and discovered that WT CFTR and PIEZO1 were in a complex together (Figure 5M).

Lastly, we found that the enhancement effect of WT CFTR on PIEZO1 function was attenuated when CFTR was maintained in a closed state by CFTRinh-172 (Figures 5N–5P). This finding suggests that both CFTR expression *and* activity are required to enhance PIEZO1 function.

We propose that CFTR, by directly interacting with PIEZO1 in a complex, stabilizes and enhances its function. This could have important ramifications because changes in the kinetics of PIEZO1 have been associated with disorders such as xerocytosis.[108,109] Therefore, it is crucial to better understand CFTR's modulatory effects on PIEZO1. The next step in doing so should be identifying which domains of CFTR and PIEZO interact and whether or not a scaffolding protein is involved.

Model of endothelial barrier failure in CF

We propose a mechanism of loss of endothelial barrier integrity in CF, which is detailed in Figure 6.

In the *healthy endothelium*, functional CFTR and PIEZO1 directly interact at the cell membrane via unknown domains (Figure 6A). This inter-action stabilizes PIEZO1 and enhances its function. SS activates PIEZO1, which leads to a transient rise in calcium[41] (Figure 6B). Transient calcium elevation activates calcium-dependent cytosolic phospholipase A2 (cPLA2)[41,110] (Figure 6C), which results in downstream processes associated with PIEZO1; examples of downstream processes are EC flow alignment and angiogenesis/wound repair in response to injuries.[25–27,106]

In *CF disease*, mutant CFTR, such as F508del-CFTR, is retained in the ER and quickly degraded, which limits the enhancing interaction with PIEZO1 (Figure 6D). However, we suspect that cPLA2 might still be activated by some other mechanisms such as calcium release from

Figure 7. Proposed model of small pulmonary blood vessel loss in CF
Loss of functional CFTR in the lung vasculature leads to altered gene expression, loss of CFTR-PIEZO1 interaction, and altered lipid metabolism that leads to the overactivation of TRPV4. Consequently, endothelial barrier integrity is compromised, and angiogenesis is impaired; as a result, loss of small pulmonary blood vessels occurs in CF.

intracellular stores,[111–113] independently of PIEZO1 (Figure 6E). In fact, it has been reported that AA-induced lipid peroxidation can lead to increased release of calcium from intracellular stores and increased PLA2 activation; this does not depend on increased influx from extracellular calcium[113] (e.g., through PIEZO1). Our data report that AA is increased in CFTR-deficient cells (Figure 4B). Furthermore, CF is associated with ER-stress-induced calcium release due to the unfolded protein response (UPR).[112] Altogether, these could explain how cPLA2 gets activated independently of PIEZO1.

Activated cPLA2 would preferably hydrolyze AA-containing membrane-bound phospholipids and free AA[110,114,115] (Figure 6F). EPA, on the other hand, would preferably be freed by calcium-independent iPLA2[100] (Figure 6G). In *CF disease*, the membrane is richer in AA and EPA compared to a *healthy state*,[68,70,93,95–99] which likely results in increased free AA and EPA. Free AA and EPA would then be converted into their respective metabolites 5′6′-EET and 17′18′-EEQ (Figure 6H) and incorporated back into the membrane (Figure 6I), where they would lower the activation threshold of or even directly activate TRPV4.[63,64,101,102,105]

Consequently, for a given SS stimulus, an increased number of TRPV4 channels would get activated (Figure 6J). Sustained increase in intracellular calcium likely ensues,[41] eventually resulting in calcium overload (Figure 6K). Higher intracellular calcium levels lead to overactivation of calcium-dependent m-calpain (Figure 6L), which results in faster degradation of VE-cad and reduced expression of AJs[27,35–37,40] (Figure 6M). Loss of focal adhesion is also likely to play a role, and its involvement in the proposed mechanism requires further study.

Model of small pulmonary blood vessel loss in CF

We also propose an integrated mechanism of loss of SPBVs in CF (Figure 7) based on our findings and available literature: (1) altered gene expression, (2) loss of CFTR-PIEZO1 interaction, and (3) altered lipid metabolism leading to overactivation of TRPV4 are the key contributors to loss of barrier integrity. Eventually, barrier failure, coupled with impaired angiogenesis, is likely to be the main driving force behind the loss of SPBVs. This proposed mechanism may be the basis for the extensive vascular remodeling observed in severe CF lung disease (Figure 1A).

DISCUSSION

We have established a mechanism underlying loss of SPBVs in CF by demonstrating that CFTR directly interacts with MsC PIEZO1. Furthermore, by altering membrane lipid composition, CFTR deficiency can indirectly lead to overactivation of another MsC, namely TRPV4, which results in loss of cell-cell contact. This study paves the way for the identification of other MsCs that could be modulated by CFTR through similar mechanisms. Moreover, assessing lipid imbalances could provide insight into the degree of endothelial barrier perturbation in CF; in CF-related lung diseases such as pneumonia, interstitial lung disease, and obstructive pulmonary disease[19–21]; and in cardiac conditions. This study may inform the development of new therapeutics targeted at the endothelium in CF, CF-related, and cardiovascular diseases.

Limitations of the study

By design, this was primarily a human study that used both human primary cells and a vessel-on-a-chip model. Despite some possibilities of allometric scaling between humans and mice, SS is much higher in mice compared to humans, and it is possible that scaling error may occur.[116–118] On the other hand, our approach limited confounding variables that are typically problematic with *in vivo* studies, and most importantly, allowed us to impose static conditions. Without the ability to ensure static conditions, we would not have been able to identify the SS-dependent endothelial barrier failure associated with CFTR deficiency. Besides, the multi-channel microfluidic devices allowed us to run control and test samples concurrently in a high-throughput manner; this would not have been feasible *in vivo*. Moreover, our findings regarding the important role of TRPV4 in CF endothelial barrier failure are likely to translate *in vivo*; in fact, a very recent *in vivo/ex vivo* study using the lungs of rats and mice reported that TRPV4 inhibition, as well as CFTR potentiation, helped prevent loss of endothelial barrier integrity in pneumonia, where CFTR expression is reduced.[60]

STAR★METHODS

Detailed methods are provided in the online version of this paper and include the following:

- KEY RESOURCES TABLE
- RESOURCE AVAILABILITY
  - Lead contact
  - Materials availability
  - Data and code availability
- EXPERIMENTAL MODEL AND STUDY PARTICIPANT DETAILS
  - Primary cells
  - Cell line
  - Human subjects
- METHOD DETAILS
  - Computerized Tomography
  - Pulmonary vascular morphometry
  - Cell transfection
  - Microfluidics studies
  - Calcium removal and supplementation
  - Calcium imaging
  - Calpain activity assay
  - Fluorescence Microscopy
  - Fluorescence anisotropy
  - RNA Extraction for Bulk-RNA sequencing
  - Ingenuity pathway analysis
  - Lipid analysis
  - Patch clamping
  - Co-immunoprecipitation
  - Tube formation assay
- QUANTIFICATION AND STATISTICAL ANALYSIS

SUPPLEMENTAL INFORMATION

Supplemental information can be found online at https://doi.org/10.1016/j.isci.2024.110703.

AUTHOR CONTRIBUTIONS

A.P.N. and J.-P.A. designed experiments and wrote the paper. J.L. performed all patch-clamping experiments. R.A. recruited CF patients and collected computerized tomography scans. G.M. performed pulmonary vascular morphometry analysis. P.L. and J.-P.A. performed RNA-sequencing analysis. J.-P.A. performed all other experiments. K.A. performed ingenuity pathway analysis, edited the manuscript, and provided feedback. A.K. provided knowledge of lipid metabolism and suggestions regarding experimental details. All authors read and approved the final manuscript.

DECLARATION OF INTERESTS

The authors declare no competing interests.

REFERENCES

1. Saint-Criq, V., and Gray, M.A. (2017). Role of CFTR in epithelial physiology. Cell. Mol. Life Sci. 74, 93–115. https://doi.org/10.1007/s00018-016-2391-y.

2. Tousson, A., Van Tine, B.A., Naren, A.P., Shaw, G.M., and Schwiebert, L.M. (1998). Characterization of CFTR expression and chloride channel activity in human endothelia. Am. J. Physiol. 275, C1555–C1564. https://doi.org/10.1152/ajpcell.1998.275.6.C1555.

3. Kuo, W., de Bruijne, M., Petersen, J., Nasserinejad, K., Ozturk, H., Chen, Y., Perez-Rovira, A., and Tiddens, H.A.W.M. (2017). Diagnosis of bronchiectasis and airway wall thickening in children with cystic fibrosis: Objective airway-artery quantification. Eur. Radiol. 27, 4680–4689. https://doi.org/10.1007/s00330-017-4819-7.

4. Wielpütz, M.O., Puderbach, M., Kopp-Schneider, A., Stahl, M., Fritzsching, E., Sommerburg, O., Ley, S., Sumkauskaite, M., Biederer, J., Kauczor, H.-U., et al. (2014). Magnetic Resonance Imaging Detects Changes in Structure and Perfusion, and Response to Therapy in Early Cystic Fibrosis Lung Disease. Am. J. Respir. Crit. Care Med. 189, 956–965. https://doi.org/10.1164/rccm.201309-1659OC.

5. Buehler, T., Steinmann, M., Singer, F., Regamey, N., Casaulta, C., Schoeni, M.H., and Simonetti, G.D. (2012). Increased arterial stiffness in children with cystic fibrosis. Eur. Respir. J. 39, 1536–1537. https://doi.org/10.1183/09031936.00212511.

6. Totani, L., Plebani, R., Piccoli, A., Di Silvestre, S., Lanuti, P., Recchiuti, A., Cianci, E., Dell'Elba, G., Sacchetti, S., Patruno, S., et al. (2017). Mechanisms of endothelial cell dysfunction in cystic fibrosis. Biochim. Biophys. Acta, Mol. Basis Dis. 1863, 3243–3253. https://doi.org/10.1016/j.bbadis.2017.08.011.

7. Bradley, S., Solin, P., Wilson, J., Johns, D., Walters, E.H., and Naughton, M.T. (1999). Hypoxemia and Hypercapnia During Exercise and Sleep in Patients With Cystic Fibrosis. Chest 116, 647–654. https://doi.org/10.1378/chest.116.3.647.

8. Betancourt, M., Slade, G., and Dinwiddie, R. (1991). Oxygen saturation in cystic fibrosis. Arch. Dis. Child. 66, 1075–1076. https://doi.org/10.1136/adc.66.9.1075.

9. Hsu, P.-P., Li, S., Li, Y.-S., Usami, S., Ratcliffe, A., Wang, X., and Chien, S. (2001). Effects of Flow Patterns on Endothelial Cell Migration into a Zone of Mechanical Denudation. Biochem. Biophys. Res. Commun. 285, 751–759. https://doi.org/10.1006/bbrc.2001.5221.

10. Levesque, M.J., Nerem, R.M., and Sprague, E.A. (1990). Vascular endothelial cell proliferation in culture and the influence of flow. Biomaterials 11, 702–707. https://doi.org/10.1016/0142-9612(90)90031-K.

11. Davies, P.F., Remuzzi, A., Gordon, E.J., Dewey, C.F., and Gimbrone, M.A. (1986). Turbulent fluid shear stress induces vascular endothelial cell turnover in vitro. Proc. Natl. Acad. Sci. USA 83, 2114–2117. https://doi.org/10.1073/pnas.83.7.2114.

12. Corson, M.A., James, N.L., Latta, S.E., Nerem, R.M., Berk, B.C., and Harrison, D.G. (1996). Phosphorylation of endothelial nitric oxide synthase in response to fluid shear stress. Circ. Res. 79, 984–991. https://doi.org/10.1161/01.res.79.5.984.

13. Dewey, C.F., Jr., Bussolari, S.R., Gimbrone, M.A., Jr., and Davies, P.F. (1981). The Dynamic Response of Vascular Endothelial Cells to Fluid Shear Stress. J. Biomech. Eng. 103, 177–185. https://doi.org/10.1115/1.3138276.

14. Dickinson, M.G., Bartelds, B., Borgdorff, M.A.J., and Berger, R.M.F. (2013). The role of disturbed blood flow in the development of pulmonary arterial hypertension: lessons from preclinical animal models. Am. J. Physiol. Lung Cell Mol. Physiol. 305, L1–L14. https://doi.org/10.1152/ajplung.00031.2013.

15. Tang, B.T., Pickard, S.S., Chan, F.P., Tsao, P.S., Taylor, C.A., and Feinstein, J.A. (2012). Wall Shear Stress is Decreased in the Pulmonary Arteries of Patients with Pulmonary Arterial Hypertension: An Image-Based, Computational Fluid Dynamics Study. Pulm. Circ. 2, 470–476. https://doi.org/10.4103/2045-8932.105035.

16. Hueper, K., Vogel-Claussen, J., Parikh, M.A., Austin, J.H.M., Bluemke, D.A., Carr, J., Choi, J., Goldstein, T.A., Gomes, A.S., Hoffman, E.A., et al. (2015). Pulmonary Microvascular Blood Flow in Mild Chronic Obstructive Pulmonary Disease and Emphysema. The MESA COPD Study. Am. J. Respir. Crit. Care Med. 192, 570–580. https://doi.org/10.1164/rccm.201411-2120OC.

17. Sakao, S., Voelkel, N.F., and Tatsumi, K. (2014). The vascular bed in COPD: pulmonary hypertension and pulmonary vascular alterations. Eur. Respir. Rev. 23, 350–355. https://doi.org/10.1183/09059180.00007913.

18. Matsuoka, S., Washko, G.R., Yamashiro, T., Estepar, R.S.J., Diaz, A., Silverman, E.K., Hoffman, E., Fessler, H.E., Criner, G.J., Marchetti, N., et al. (2010). Pulmonary Hypertension and Computed Tomography Measurement of Small Pulmonary Vessels in Severe Emphysema. Am. J. Respir. Crit. Care Med. 181, 218–225. https://doi.org/10.1164/rccm.200908-1189OC.

19. Rab, A., Rowe, S.M., Raju, S.V., Bebok, Z., Matalon, S., and Collawn, J.F. (2013). Cigarette smoke and CFTR: implications in the pathogenesis of COPD. Am. J. Physiol. Lung Cell Mol. Physiol. 305, L530–L541.

20. Raju, S.V., Solomon, G.M., Dransfield, M.T., and Rowe, S.M. (2016). Acquired Cystic Fibrosis Transmembrane Conductance Regulator Dysfunction in Chronic Bronchitis and Other Diseases of Mucus Clearance. Clin. Chest Med. 37, 147–158. https://doi.org/10.1016/j.ccm.2015.11.003.

21. Wellmerling, J.H., Chang, S.-W., Kim, E., Osman, W.H., Boyaka, P.N., Borchers, M.T., and Cormet-Boyaka, E. (2019). Reduced expression of the Ion channel CFTR contributes to airspace enlargement as a consequence of aging and in response to cigarette smoke in mice. Respir. Res. 20, 200. https://doi.org/10.1186/s12931-019-1170-3.

22. Campinho, P., Vilfan, A., and Vermot, J. (2020). Blood Flow Forces in Shaping the Vascular System: A Focus on Endothelial Cell Behavior. Front. Physiol. 11, 552.

23. Kochhan, E., Lenard, A., Ellertsdottir, E., Herwig, L., Affolter, M., Belting, H.-G., and Siekmann, A.F. (2013). Blood Flow Changes Coincide with Cellular Rearrangements during Blood Vessel Pruning in Zebrafish Embryos. PLoS One 8, e75060-.

24. Moses, S.R., Adorno, J.J., Palmer, A.F., and Song, J.W. (2021). Vessel-on-a-chip models for studying microvascular physiology, transport, and function in vitro. Am. J. Physiol. Cell Physiol. 320, C92–C105. https://doi.org/10.1152/ajpcell.00355.2020.

25. Atcha, H., Jairaman, A., Holt, J.R., Meli, V.S., Nagalla, R.R., Veerasubramanian, P.K., Brumm, K.T., Lim, H.E., Othy, S., Cahalan, M.D., et al. (2021). Mechanically activated ion channel Piezo1 modulates macrophage polarization and stiffness sensing. Nat. Commun. 12, 3256. https://doi.org/10.1038/s41467-021-23482-5.

26. Zechini, L., Amato, C., Scopelliti, A., and Wood, W. (2022). Piezo acts as a molecular brake on wound closure to ensure effective inflammation and maintenance of epithelial integrity. Curr. Biol. 32, 3584–3592.e4. https://doi.org/10.1016/j.cub.2022.06.041.

27. Li, J., Hou, B., Tumova, S., Muraki, K., Bruns, A., Ludlow, M.J., Sedo, A., Hyman, A.J., McKeown, L., Young, R.S., et al. (2014). Piezo1 integration of vascular architecture with physiological force. Nature 515, 279–282. https://doi.org/10.1038/nature13701.

28. Li, M., Stenmark, K.R., Shandas, R., and Tan, W. (2009). Effects of Pathological Flow on Pulmonary Artery Endothelial Production of Vasoactive Mediators and Growth Factors. J. Vasc. Res. 46, 561–571. https://doi.org/10.1159/000226224.

29. Venuta, F., Rendina, E.A., Rocca, G.D., De Giacomo, T., Pugliese, F., Ciccone, A.M., Vizza, C.D., and Coloni, G.F. (2000). Pulmonary hemodynamics contribute to

indicate priority for lung transplantation in patients with cystic fibrosis. J. Thorac. Cardiovasc. Surg. *119*, 682–689. https://doi.org/10.1016/S0022-5223(00)70002-X.

30. Venuta, F., Tonelli, A.R., Anile, M., Diso, D., de Giacomo, T., Ruberto, F., Russo, E., Rolla, M., Quattrucci, S., Rendina, E.A., et al. (2012). Pulmonary hypertension is associated with higher mortality in cystic fibrosis patients awaiting lung transplantation. J. Cardiovasc. Surg. *53*, 817–820.

31. Belle-van Meerkerk, G., Cramer, M.J., Kwakkel-van Erp, J.M., Nugroho, M.A., Tahri, S., de Valk, H.W., and van de Graaf, E.A. (2013). Pulmonary hypertension is a mild comorbidity in end-stage cystic fibrosis patients. J. Heart Lung Transplant. *32*, 609–614. https://doi.org/10.1016/j.healun.2013.03.006.

32. Lau, E.M.T., Giannoulatou, E., Celermajer, D.S., and Humbert, M. (2017). Epidemiology and treatment of pulmonary arterial hypertension. Nat. Rev. Cardiol. *14*, 603–614. https://doi.org/10.1038/nrcardio.2017.84.

33. Szulcek, R., Happé, C.M., Rol, N., Fontijn, R.D., Dickhoff, C., Hartemink, K.J., Grünberg, K., Tu, L., Timens, W., Nossent, G.D., et al. (2016). Delayed Microvascular Shear Adaptation in Pulmonary Arterial Hypertension. Role of Platelet Endothelial Cell Adhesion Molecule-1 Cleavage. Am. J. Respir. Crit. Care Med. *193*, 1410–1420. https://doi.org/10.1164/rccm.201506-1231OC.

34. Melis, N., Tauc, M., Cougnon, M., Bendahhou, S., Giuliano, S., Rubera, I., and Duranton, C. (2014). Revisiting CFTR inhibition: a comparative study of CFTRinh-172 and GlyH-101 inhibitors. Br. J. Pharmacol. *171*, 3716–3727. https://doi.org/10.1111/bph.12726.

35. Woodcock, S.A., Rooney, C., Liontos, M., Connolly, Y., Zoumpourlis, V., Whetton, A.D., Gorgoulis, V.G., and Malliri, A. (2009). Src-Induced Disassembly of Adherens Junctions Requires Localized Phosphorylation and Degradation of the Rac Activator Tiam1. Mol. Cell *33*, 639–653. https://doi.org/10.1016/j.molcel.2009.02.012.

36. Miyazaki, T., Taketomi, Y., Takimoto, M., Lei, X.-F., Arita, S., Kim-Kaneyama, J.R., Arata, S., Ohata, H., Ota, H., Murakami, M., and Miyazaki, A. (2011). m-Calpain Induction in Vascular Endothelial Cells on Human and Mouse Atheromas and Its Roles in VE-Cadherin Disorganization and Atherosclerosis. Circulation *124*, 2522–2532. https://doi.org/10.1161/CIRCULATIONAHA.111.021675.

37. Rios-Doria, J., Day, K.C., Kuefer, R., Rashid, M.G., Chinnaiyan, A.M., Rubin, M.A., and Day, M.L. (2003). The Role of Calpain in the Proteolytic Cleavage of E-cadherin in Prostate and Mammary Epithelial Cells. J. Biol. Chem. *278*, 1372–1379. https://doi.org/10.1074/jbc.M208772200.

38. Zhang, Y., Liu, N.M., Wang, Y., Youn, J.Y., and Cai, H. (2017). Endothelial cell calpain as a critical modulator of angiogenesis. Biochim. Biophys. Acta, Mol. Basis Dis. *1863*, 1326–1335. https://doi.org/10.1016/j.bbadis.2017.03.021.

39. Goll, D.E., Thompson, V.F., Li, H., Wei, W., and Cong, J. (2003). The Calpain System. Physiol. Rev. *83*, 731–801. https://doi.org/10.1152/physrev.00029.2002.

40. Miyazaki, T., Honda, K., and Ohata, H. (2007). Requirement of Ca2+ influx- and phosphatidylinositol 3-kinase-mediated m-calpain activity for shear stress-induced endothelial cell polarity. Am. J. Physiol. Cell Physiol. *293*, C1216–C1225. https://doi.org/10.1152/ajpcell.00083.2007.

41. Swain, S.M., and Liddle, R.A. (2021). Piezo1 acts upstream of TRPV4 to induce pathological changes in endothelial cells due to shear stress. J. Biol. Chem. *296*, 100171. https://doi.org/10.1074/jbc.RA120.015059.

42. Rosser, B.G., Powers, S.P., and Gores, G.J. (1993). Calpain activity increases in hepatocytes following addition of ATP. Demonstration by a novel fluorescent approach. J. Biol. Chem. *268*, 23593–23600. https://doi.org/10.1016/S0021-9258(19)49504-5.

43. Hanna, R.A., Campbell, R.L., and Davies, P.L. (2008). Calcium-bound structure of calpain and its mechanism of inhibition by calpastatin. Nature *456*, 409–412. https://doi.org/10.1038/nature07451.

44. Coste, B., Murthy, S.E., Mathur, J., Schmidt, M., Mechioukhi, Y., Delmas, P., and Patapoutian, A. (2015). Piezo1 ion channel pore properties are dictated by C-terminal region. Nat. Commun. *6*, 7223. https://doi.org/10.1038/ncomms8223.

45. Botello-Smith, W.M., Jiang, W., Zhang, H., Ozkan, A.D., Lin, Y.-C., Pham, C.N., Lacroix, J.J., and Luo, Y. (2019). A mechanism for the activation of the mechanosensitive Piezo1 channel by the small molecule Yoda1. Nat. Commun. *10*, 4503. https://doi.org/10.1038/s41467-019-12501-1.

46. Ranade, S.S., Qiu, Z., Woo, S.-H., Hur, S.S., Murthy, S.E., Cahalan, S.M., Xu, J., Mathur, J., Bandell, M., Coste, B., et al. (2014). Piezo1, a mechanically activated ion channel, is required for vascular development in mice. Proc. Natl. Acad. Sci. USA *111*, 10347–10352. https://doi.org/10.1073/pnas.1409233111.

47. Nilius, B., Vriens, J., Prenen, J., Droogmans, G., and Voets, T. (2004). TRPV4 calcium entry channel: a paradigm for gating diversity. Am. J. Physiol. Cell Physiol. *286*, C195–C205. https://doi.org/10.1152/ajpcell.00365.2003.

48. Gao, X., Wu, L., and O'Neil, R.G. (2003). Temperature-modulated Diversity of TRPV4 Channel Gating: activation by physical stresses and phorbol ester derivatives through protein kinase C-dependent and -independent pathways. J. Biol. Chem. *278*, 27129–27137. https://doi.org/10.1074/jbc.M302517200.

49. Suzuki, M., Mizuno, A., Kodaira, K., and Imai, M. (2003). Impaired Pressure Sensation in Mice Lacking TRPV4. J. Biol. Chem. *278*, 22664–22668. https://doi.org/10.1074/jbc.M302561200.

50. Liedtke, W., Tobin, D.M., Bargmann, C.I., and Friedman, J.M. (2003). Mammalian TRPV4 (VR-OAC) directs behavioral responses to osmotic and mechanical stimuli in Caenorhabditis elegans. Proc. Natl. Acad. Sci. USA *100*, 14531–14536. https://doi.org/10.1073/pnas.2235619100.

51. Syeda, R., Xu, J., Dubin, A.E., Coste, B., Mathur, J., Huynh, T., Matzen, J., Lao, J., Tully, D.C., Engels, I.H., et al. (2015). Chemical activation of the mechanotransduction channel Piezo1. Elife *4*, e07369. https://doi.org/10.7554/eLife.07369.

52. Bae, C., Sachs, F., and Gottlieb, P.A. (2011). The mechanosensitive ion channel Piezo1 is inhibited by the peptide GsMTx4. Biochemistry *50*, 6295–6300. https://doi.org/10.1021/BI200770Q.

53. Wu, S., Jian, M.-Y., Xu, Y.-C., Zhou, C., Al-Mehdi, A.-B., Liedtke, W., Shin, H.-S., and Townsley, M.I. (2009). Ca2+ entry via α1G and TRPV4 channels differentially regulates surface expression of P-selectin and barrier integrity in pulmonary capillary endothelium. Am. J. Physiol. Lung Cell Mol. Physiol. *297*, L650–L657. https://doi.org/10.1152/ajplung.00015.2009.

54. Phuong, T.T.T., Redmon, S.N., Yarishkin, O., Winter, J.M., Li, D.Y., and Križaj, D. (2017). Calcium influx through TRPV4 channels modulates the adherens contacts between retinal microvascular endothelial cells. J. Physiol. *595*, 6869–6885. https://doi.org/10.1113/JP275052.

55. Willette, R.N., Bao, W., Nerurkar, S., Yue, T.L., Doe, C.P., Stankus, G., Turner, G.H., Ju, H., Thomas, H., Fishman, C.E., et al. (2008). Systemic Activation of the Transient Receptor Potential Vanilloid Subtype 4 Channel Causes Endothelial Failure and Circulatory Collapse: Part 2. J. Pharmacol. Exp. Therapeut. *326*, 443–452. https://doi.org/10.1124/jpet.107.134551.

56. Thorneloe, K.S., Sulpizio, A.C., Lin, Z., Figueroa, D.J., Clouse, A.K., McCafferty, G.P., Chendrimada, T.P., Lashinger, E.S.R., Gordon, E., Evans, L., et al. (2008). N-((1S)-1-{[4-((2S)-2-{[(2,4-Dichlorophenyl)sulfonyl]amino}-3-hydroxypropanoyl)-1-piperazinyl]carbonyl}-3-methylbutyl)-1-benzothiophene-2-carboxamide (GSK1016790A), a Novel and Potent Transient Receptor Potential Vanilloid 4 Channel Agonist Induces Urinary Bladder Contraction and Hyperactivity: Part I. J. Pharmacol. Exp. Therapeut. *326*, 432–442. https://doi.org/10.1124/jpet.108.139295.

57. Jin, M., Wu, Z., Chen, L., Jaimes, J., Collins, D., Walters, E.T., and O'Neil, R.G. (2011). Determinants of TRPV4 Activity following Selective Activation by Small Molecule Agonist GSK1016790A. PLoS One *6*, e16713-.

58. Everaerts, W., Zhen, X., Ghosh, D., Vriens, J., Gevaert, T., Gilbert, J.P., Hayward, N.J., McNamara, C.R., Xue, F., Moran, M.M., et al. (2010). Inhibition of the cation channel TRPV4 improves bladder function in mice and rats with cyclophosphamide-induced cystitis. Proc. Natl. Acad. Sci. USA *107*, 19084–19089. https://doi.org/10.1073/pnas.1005333107.

59. Peng, S., Grace, M.S., Gondin, A.B., Retamal, J.S., Dill, L., Darby, W., Bunnett, N.W., Abogadie, F.C., Carbone, S.E., Tigani, T., et al. (2020). The transient receptor potential vanilloid 4 (TRPV4) ion channel mediates protease activated receptor 1 (PAR1)-induced vascular hyperpermeability. Lab. Invest. *100*, 1057–1067. https://doi.org/10.1038/s41374-020-0430-7.

60. Erfinanda, L., Zou, L., Gutbier, B., Kneller, L., Weidenfeld, S., Michalick, L., Lei, D., Reppe, K., Teixeira Alves, L.G., Schneider, B., et al. (2022). Loss of endothelial CFTR drives barrier failure and edema formation in lung infection and can be targeted by CFTR potentiation. Sci. Transl. Med. *14*, eabg8577. https://doi.org/10.1126/scitranslmed.abg8577.

61. Qi, Y., Andolfi, L., Frattini, F., Mayer, F., Lazzarino, M., and Hu, J. (2015). Membrane stiffening by STOML3 facilitates mechanosensation in sensory neurons. Nat.

Commun. 6, 8512. https://doi.org/10.1038/ncomms9512.

62. Cox, C.D., Bae, C., Ziegler, L., Hartley, S., Nikolova-Krstevski, V., Rohde, P.R., Ng, C.-A., Sachs, F., Gottlieb, P.A., and Martinac, B. (2016). Removal of the mechanoprotective influence of the cytoskeleton reveals PIEZO1 is gated by bilayer tension. Nat. Commun. 7, 10366. https://doi.org/10.1038/ncomms10366.

63. Romero, L.O., Massey, A.E., Mata-Daboin, A.D., Sierra-Valdez, F.J., Chauhan, S.C., Cordero-Morales, J.F., and Vásquez, V. (2019). Dietary fatty acids fine-tune Piezo1 mechanical response. Nat. Commun. 10, 1200. https://doi.org/10.1038/s41467-019-09055-7.

64. Caires, R., Sierra-Valdez, F.J., Millet, J.R.M., Herwig, J.D., Roan, E., Vásquez, V., and Cordero-Morales, J.F. (2017). Omega-3 Fatty Acids Modulate TRPV4 Function through Plasma Membrane Remodeling. Cell Rep. 21, 246–258. https://doi.org/10.1016/j.celrep.2017.09.029.

65. Vásquez, V., Krieg, M., Lockhead, D., and Goodman, M.B. (2014). Phospholipids that Contain Polyunsaturated Fatty Acids Enhance Neuronal Cell Mechanics and Touch Sensation. Cell Rep. 6, 70–80. https://doi.org/10.1016/j.celrep.2013.12.012.

66. Harayama, T., and Riezman, H. (2018). Understanding the diversity of membrane lipid composition. Nat. Rev. Mol. Cell Biol. 19, 281–296. https://doi.org/10.1038/nrm.2017.138.

67. Sezgin, E., Levental, I., Mayor, S., and Eggeling, C. (2017). The mystery of membrane organization: composition, regulation and roles of lipid rafts. Nat. Rev. Mol. Cell Biol. 18, 361–374. https://doi.org/10.1038/nrm.2017.16.

68. Hamai, H., Keyserman, F., Quittell, L.M., and Worgall, T.S. (2009). Defective CFTR increases synthesis and mass of sphingolipids that modulate membrane composition and lipid signaling. J. Lipid Res. 50, 1101–1108. https://doi.org/10.1194/jlr.M800427-JLR200.

69. Lee, M.-J., Thangada, S., Claffey, K.P., Ancellin, N., Liu, C.H., Kluk, M., Volpi, M., Sha'afi, R.I., and Hla, T. (1999). Vascular Endothelial Cell Adherens Junction Assembly and Morphogenesis Induced by Sphingosine-1-Phosphate. Cell 99, 301–312. https://doi.org/10.1016/S0092-8674(00)81661-X.

70. Boujaoude, L.C., Bradshaw-Wilder, C., Mao, C., Cohn, J., Ogretmen, B., Hannun, Y.A., and Obeid, L.M. (2001). Cystic Fibrosis Transmembrane Regulator Regulates Uptake of Sphingoid Base Phosphates and Lysophosphatidic Acid: modulation of cellular activity of sphingosine 1-phosphate. J. Biol. Chem. 276, 35258–35264. https://doi.org/10.1074/jbc.M105442200.

71. Garcia, J.G., Liu, F., Verin, A.D., Birukova, A., Dechert, M.A., Gerthoffer, W.T., Bamberg, J.R., and English, D. (2001). Sphingosine 1-phosphate promotes endothelial cell barrier integrity by Edg-dependent cytoskeletal rearrangement. J. Clin. Invest. 108, 689–701. https://doi.org/10.1172/JCI12450.

72. Meissner, A., Yang, J., Kroetsch, J.T., Sauvé, M., Dax, H., Momen, A., Noyan-Ashraf, M.H., Heximer, S., Husain, M., Lidington, D., and Bolz, S.S. (2012). Tumor Necrosis Factor-α–Mediated Downregulation of the

Cystic Fibrosis Transmembrane Conductance Regulator Drives Pathological Sphingosine-1-Phosphate Signaling in a Mouse Model of Heart Failure. Circulation 125, 2739–2750. https://doi.org/10.1161/CIRCULATIONAHA.111.047316.

73. Brown, M.B., Hunt, W.R., Noe, J.E., Rush, N.I., Schweitzer, K.S., Leece, T.C., Moldobaeva, A., Wagner, E.M., Dudek, S.M., Poirier, C., et al. (2014). Loss of Cystic Fibrosis Transmembrane Conductance Regulator Impairs Lung Endothelial Cell Barrier Function and Increases Susceptibility to Microvascular Damage from Cigarette Smoke. Pulm. Circ. 4, 260–268. https://doi.org/10.1086/675989.

74. Xiao, K., Oas, R.G., Chiasson, C.M., and Kowalczyk, A.P. (2007). Role of p120-catenin in cadherin trafficking. Biochim. Biophys. Acta 1773, 8–16. https://doi.org/10.1016/j.bbamcr.2006.07.005.

75. Tzima, E., Irani-Tehrani, M., Kiosses, W.B., Dejana, E., Schultz, D.A., Engelhardt, B., Cao, G., DeLisser, H., and Schwartz, M.A. (2005). A mechanosensory complex that mediates the endothelial cell response to fluid shear stress. Nature 437, 426–431. https://doi.org/10.1038/nature03952.

76. Coon, B.G., Baeyens, N., Han, J., Budatha, M., Ross, T.D., Fang, J.S., Yun, S., Thomas, J.-L., and Schwartz, M.A. (2015). Intramembrane binding of VE-cadherin to VEGFR2 and VEGFR3 assembles the endothelial mechanosensory complex. J. Cell Biol. 208, 975–986. https://doi.org/10.1083/jcb.201408103.

77. Gerhardt, H., Golding, M., Fruttiger, M., Ruhrberg, C., Lundkvist, A., Abramsson, A., Jeltsch, M., Mitchell, C., Alitalo, K., Shima, D., and Betsholtz, C. (2003). VEGF guides angiogenic sprouting utilizing endothelial tip cell filopodia. J. Cell Biol. 161, 1163–1177. https://doi.org/10.1083/jcb.200302047.

78. McColley, S.A., Stellmach, V., Boas, S.R., Jain, M., and Crawford, S.E. (2000). Serum Vascular Endothelial Growth Factor Is Elevated in Cystic Fibrosis and Decreases with Treatment of Acute Pulmonary Exacerbation. Am. J. Respir. Crit. Care Med. 161, 1877–1880. https://doi.org/10.1164/ajrccm.161.6.9905022.

79. Amoakon, J.-P., Mylavarapu, G., Amin, R.S., and Naren, A.P. (2024). Pulmonary Vascular Dysfunctions in Cystic Fibrosis. Physiology 39, 179–192. https://doi.org/10.1152/physiol.00024.2023.

80. Baratchi, S., Knoerzer, M., Khoshmanesh, K., Mitchell, A., and McIntyre, P. (2017). Shear Stress Regulates TRPV4 Channel Clustering and Translocation from Adherens Junctions to the Basal Membrane. Sci. Rep. 7, 15942. https://doi.org/10.1038/s41598-017-16276-7.

81. Verhaeghe, C., Tabruyn, S.P., Oury, C., Bours, V., and Griffioen, A.W. (2007). Intrinsic pro-angiogenic status of cystic fibrosis airway epithelial cells. Biochem. Biophys. Res. Commun. 356, 745–749. https://doi.org/10.1016/j.bbrc.2007.02.166.

82. Osborn, E.A., Rabodzey, A., Dewey, C.F., and Hartwig, J.H. (2006). Endothelial actin cytoskeleton remodeling during mechanostimulation with fluid shear stress. Am. J. Physiol. Cell Physiol. 290, C444–C452. https://doi.org/10.1152/ajpcell.00218.2005.

83. Henig, N.R., Glenny, R.W., and Aitken, M.L. (1998). A hypertrophied bronchial

circulatory system may participate in gas exchange. Lancet 351, 113.

84. Davies, P.F. (1995). Flow-mediated endothelial mechanotransduction. Physiol. Rev. 75, 519–560. https://doi.org/10.1152/physrev.1995.75.3.519.

85. Wagner, E.M. (2006). Bronchial circulation. In Encyclopedia of Respiratory Medicine, G.J. Laurent and S.D. Shapiro, eds. (Academic Press), pp. 255–259. https://doi.org/10.1016/B0-12-370879-6/00503-2.

86. Birukov, K.G., Birukova, A.A., Dudek, S.M., Verin, A.D., Crow, M.T., Zhan, X., DePaola, N., and Garcia, J.G.N. (2002). Shear Stress-Mediated Cytoskeletal Remodeling and Cortactin Translocation in Pulmonary Endothelial Cells. Am. J. Respir. Cell Mol. Biol. 26, 453–464. https://doi.org/10.1165/ajrcmb.26.4.4725.

87. Swiatecka-Urban, A., Talebian, L., Kanno, E., Moreau-Marquis, S., Coutermarsh, B., Hansen, K., Karlson, K.H., Barnaby, R., Cheney, R.E., Langford, G.M., et al. (2007). Myosin Vb Is Required for Trafficking of the Cystic Fibrosis Transmembrane Conductance Regulator in Rab11a-specific Apical Recycling Endosomes in Polarized Human Airway Epithelial Cells. J. Biol. Chem. 282, 23725–23736. https://doi.org/10.1074/jbc.M608531200.

88. Rodal, A.A., Tetreault, J.W., Lappalainen, P., Drubin, D.G., and Amberg, D.C. (1999). Aip1p Interacts with Cofilin to Disassemble Actin Filaments. J. Cell Biol. 145, 1251–1264. https://doi.org/10.1083/jcb.145.6.1251.

89. Okada, K., Obinata, T., and Abe, H. (1999). XAIP1: a Xenopus homologue of yeast actin interacting protein 1 (AIP1), which induces disassembly of actin filaments cooperatively with ADF/cofilin family proteins. J. Cell Sci. 112, 1553–1565. https://doi.org/10.1242/jcs.112.10.1553.

90. Chrzanowska-Wodnicka, M., and Burridge, K. (1996). Rho-stimulated contractility drives the formation of stress fibers and focal adhesions. J. Cell Biol. 133, 1403–1415. https://doi.org/10.1083/jcb.133.6.1403.

91. Oakes, P.W., Beckham, Y., Stricker, J., and Gardel, M.L. (2012). Tension is required but not sufficient for focal adhesion maturation without a stress fiber template. J. Cell Biol. 196, 363–374. https://doi.org/10.1083/jcb.201107042.

92. Case, L.B., and Waterman, C.M. (2015). Integration of actin dynamics and cell adhesion by a three-dimensional, mechanosensitive molecular clutch. Nat. Cell Biol. 17, 955–963. https://doi.org/10.1038/ncb3191.

93. Freedman, S.D., Katz, M.H., Parker, E.M., Laposata, M., Urman, M.Y., and Alvarez, J.G. (1999). A membrane lipid imbalance plays a role in the phenotypic expression of cystic fibrosis in cftr−/− mice. Proc. Natl. Acad. Sci. USA 96, 13995–14000. https://doi.org/10.1073/pnas.96.24.13995.

94. Guilbault, C., Wojewodka, G., Saeed, Z., Hajduch, M., Matouk, E., De Sanctis, J.B., and Radzioch, D. (2009). Cystic Fibrosis Fatty Acid Imbalance Is Linked to Ceramide Deficiency and Corrected by Fenretinide. Am. J. Respir. Cell Mol. Biol. 41, 100–106. https://doi.org/10.1165/rcmb.2008-0279OC.

95. Freedman, S.D., Blanco, P.G., Zaman, M.M., Shea, J.C., Ollero, M., Hopper, I.K., Weed, D.A., Gelrud, A., Regan, M.M., Laposata, M.,

et al. (2004). Association of Cystic Fibrosis with Abnormalities in Fatty Acid Metabolism. N. Engl. J. Med. *350*, 560–569. https://doi.org/10.1056/NEJMoa021218.

96. Cottrill, K.A., Farinha, C.M., and McCarty, N.A. (2020). The bidirectional relationship between CFTR and lipids. Commun. Biol. *3*, 179. https://doi.org/10.1038/s42003-020-0909-1.

97. Njoroge, S.W., Seegmiller, A.C., Katrangi, W., and Laposata, M. (2011). Increased Δ5- and Δ6-desaturase, cyclooxygenase-2, and lipoxygenase-5 expression and activity are associated with fatty acid and eicosanoid changes in cystic fibrosis. Biochim. Biophys. Acta *1811*, 431–440. https://doi.org/10.1016/j.bbalip.2011.05.002.

98. Njoroge, S.W., Laposata, M., Katrangi, W., and Seegmiller, A.C. (2012). DHA and EPA reverse cystic fibrosis-related FA abnormalities by suppressing FA desaturase expression and activity. J. Lipid Res. *53*, 257–265. https://doi.org/10.1194/jlr.M018101.

99. Andersson, C., Al-Turkmani, M.R., Savaille, J.E., Alturkmani, R., Katrangi, W., Cluette-Brown, J.E., Zaman, M.M., Laposata, M., and Freedman, S.D. (2008). Cell culture models demonstrate that CFTR dysfunction leads to defective fatty acid composition and metabolism. J. Lipid Res. *49*, 1692–1700. https://doi.org/10.1194/jlr.M700388-JLR200.

100. Abdelmagid, S.A., Clarke, S.E., Nielsen, D.E., Badawi, A., El-Sohemy, A., Mutch, D.M., and Ma, D.W.L. (2015). Comprehensive Profiling of Plasma Fatty Acid Concentrations in Young Healthy Canadian Adults. PLoS One *10*, e0116195-.

101. Watanabe, H., Vriens, J., Prenen, J., Droogmans, G., Voets, T., and Nilius, B. (2003). Anandamide and arachidonic acid use epoxyeicosatrienoic acids to activate TRPV4 channels. Nature *424*, 434–438. https://doi.org/10.1038/nature01807.

102. Berna-Erro, A., Izquierdo-Serra, M., Sepúlveda, R.V., Rubio-Moscardo, F., Doñate-Macián, P., Serra, S.A., Carrillo-Garcia, J., Perálvarez-Marín, A., González-Nilo, F., Fernández-Fernández, J.M., and Valverde, M.A. (2017). Structural determinants of 5′,6′-epoxyeicosatrienoic acid binding to and activation of TRPV4 channel. Sci. Rep. *7*, 10522. https://doi.org/10.1038/s41598-017-11274-1.

103. Vriens, J., Owsianik, G., Fisslthaler, B., Suzuki, M., Janssens, A., Voets, T., Morisseau, C., Hammock, B.D., Fleming, I., Busse, R., and Nilius, B. (2005). Modulation of the Ca2 Permeable Cation Channel TRPV4 by Cytochrome P450 Epoxygenases in Vascular Endothelium. Circ. Res. *97*, 908–915. https://doi.org/10.1161/01.RES.0000187474.47805.30.

104. Levental, K.R., Malmberg, E., Symons, J.L., Fan, Y.-Y., Chapkin, R.S., Ernst, R., and Levental, I. (2020). Lipidomic and biophysical homeostasis of mammalian membranes counteracts dietary lipid perturbations to maintain cellular fitness. Nat. Commun. *11*, 1339. https://doi.org/10.1038/s41467-020-15203-1.

105. Jacobs, M.L., Faizi, H.A., Peruzzi, J.A., Vlahovska, P.M., and Kamat, N.P. (2021). EPA and DHA differentially modulate membrane elasticity in the presence of cholesterol. Biophys. J. *120*, 2317–2329. https://doi.org/10.1016/j.bpj.2021.04.009.

106. Liu, T.T., Du, X.F., Zhang, B.B., Zi, H.X., Yan, Y., Yin, J.A., Hou, H., Gu, S.Y., Chen, Q., and Du, J.L. (2020). Piezo1-Mediated Ca2+ Activities Regulate Brain Vascular Pathfinding during Development. Neuron *108*, 180–192.e5. https://doi.org/10.1016/j.neuron.2020.07.025.

107. Huang, Y., Paul, G., Lee, J., Yarlagadda, S., McCoy, K., and Naren, A.P. (2021). Elexacaftor/Tezacaftor/Ivacaftor Improved Clinical Outcomes in a Patient with N1303K-CFTR Based on In Vitro Experimental Evidence. Am. J. Respir. Crit. Care Med. *204*, 1231–1235. https://doi.org/10.1164/rccm.202101-0090LE.

108. Andolfo, I., Alper, S.L., De Franceschi, L., Auriemma, C., Russo, R., De Falco, L., Vallefuoco, F., Esposito, M.R., Vandorpe, D.H., Shmukler, B.E., et al. (2013). Multiple clinical forms of dehydrated hereditary stomatocytosis arise from mutations in PIEZO1. Blood *121*, 3925–3935. https://doi.org/10.1182/blood-2013-02-482489.

109. Bae, C., Gnanasambandam, R., Nicolai, C., Sachs, F., and Gottlieb, P.A. (2013). Xerocytosis is caused by mutations that alter the kinetics of the mechanosensitive channel PIEZO1. Proc. Natl. Acad. Sci. USA *110*, E1162–E1168. https://doi.org/10.1073/pnas.1219777110.

110. Clark, J.D., Schievella, A.R., Nalefski, E.A., and Lin, L.-L. (1995). Cytosolic phospholipase A2. J. Lipid Mediat. Cell Signal *12*, 83–117. https://doi.org/10.1016/0929-7855(95)00012-F.

111. Philippe, R., Antigny, F., Buscaglia, P., Norez, C., Becq, F., Frieden, M., and Mignen, O. (2015). SERCA and PMCA pumps contribute to the deregulation of Ca2+ homeostasis in human CF epithelial cells. Biochim. Biophys. Acta *1853*, 892–903. https://doi.org/10.1016/j.bbamcr.2015.01.010.

112. Kerbiriou, M., Le Drévo, M.-A., Férec, C., and Trouvé, P. (2007). Coupling cystic fibrosis to endoplasmic reticulum stress: Differential role of Grp78 and ATF6. Biochim. Biophys. Acta *1772*, 1236–1249. https://doi.org/10.1016/j.bbadis.2007.10.004.

113. Caro, A.A., and Cederbaum, A.I. (2007). Role of intracellular calcium and phospholipase A2 in arachidonic acid-induced toxicity in liver cells overexpressing CYP2E1. Arch. Biochem. Biophys. *457*, 252–263. https://doi.org/10.1016/J.ABB.2006.10.018.

114. Hayashi, D., Mouchlis, V.D., and Dennis, E.A. (2021). Omega-3 versus Omega-6 fatty acid availability is controlled by hydrophobic site geometries of phospholipase A2s. J. Lipid Res. *62*, 100113. https://doi.org/10.1016/j.jlr.2021.100113.

115. Clark, J.D., Lin, L.-L., Kriz, R.W., Ramesha, C.S., Sultzman, L.A., Lin, A.Y., Milona, N., and Knopf, J.L. (1991). A novel arachidonic acid-selective cytosolic PLA2 contains a Ca2+-dependent translocation domain with homology to PKC and GAP. Cell *65*, 1043–1051. https://doi.org/10.1016/0092-8674(91)90556-E.

116. Chiu, J.-J., and Chien, S. (2011). Effects of disturbed flow on vascular endothelium: pathophysiological basis and clinical perspectives. Physiol. Rev. *91*, 327–387. https://doi.org/10.1152/physrev.00047.2009.

117. Greve, J.M., Les, A.S., Tang, B.T., Draney Blomme, M.T., Wilson, N.M., Dalman, R.L., Pelc, N.J., and Taylor, C.A. (2006). Allometric scaling of wall shear stress from mice to humans: quantification using cine phase-contrast MRI and computational fluid dynamics. Am. J. Physiol. Heart Circ. Phys. *291*, H1700–H1708. https://doi.org/10.1152/ajpheart.00274.2006.

118. Suo, J., Ferrara, D.E., Sorescu, D., Guldberg, R.E., Taylor, W.R., and Giddens, D.P. (2007). Hemodynamic Shear Stresses in Mouse Aortas. Arterioscler Thromb. Vasc. Biol. *27*, 346–351. https://doi.org/10.1161/01.ATV.0000253492.45717.46.

119. Yarlagadda, S., Zhang, W., Penmatsa, H., Ren, A., Arora, K., Naren, A.P., Khan, F.A.I., Donnellan, C.A., Srinivasan, S., Stokes, D.C., and Kappes, J.C. (2012). A Young Hispanic with c.1646G>A Mutation Exhibits Severe Cystic Fibrosis Lung Disease: Is Ivacaftor an Option for Therapy? Am. J. Respir. Crit. Care Med. *186*, 694–696. https://doi.org/10.1164/ajrccm.186.7.694.

120. Coste, B., Mathur, J., Schmidt, M., Earley, T.J., Ranade, S., Petrus, M.J., Dubin, A.E., and Patapoutian, A. (2010). Piezo1 and Piezo2 Are Essential Components of Distinct Mechanically Activated Cation Channels. Science *330*, 55–60. https://doi.org/10.1126/science.1193270.

121. Chuntharpursat-Bon, E., Povstyan, O.V., Ludlow, M.J., Carrier, D.J., Debant, M., Shi, J., Gaunt, H.J., Bauer, C.C., Curd, A., Simon Futers, T., et al. (2023). PIEZO1 and PECAM1 interact at cell-cell junctions and partner in endothelial force sensing. Commun. Biol. *6*, 358. https://doi.org/10.1038/s42003-023-04706-4.

122. Schindelin, J., Arganda-Carreras, I., Frise, E., Kaynig, V., Longair, M., Pietzsch, T., Preibisch, S., Rueden, C., Saalfeld, S., Schmid, B., et al. (2012). Fiji: an open-source platform for biological-image analysis. Nat. Methods *9*, 676–682. https://doi.org/10.1038/nmeth.2019.

123. Kindlmann, G.L., San José Estépar, R., Smith, S.M., and Westin, C.-F. (2009). Sampling and Visualizing Creases with Scale-Space Particles. IEEE Trans. Vis. Comput. Graph. *15*, 1415–1424. https://doi.org/10.1109/TVCG.2009.177.

124. Lindeberg, T. (1998). Edge Detection and Ridge Detection with Automatic Scale Selection. Int. J. Comput. Vis. *30*, 117–156. https://doi.org/10.1023/A:1008097225773.

125. Coche, E., Pawlak, S., Dechambre, S., and Maldague, B. (2003). Peripheral pulmonary arteries: identification at multi-slice spiral CT with 3D reconstruction. Eur. Radiol. *13*, 815–822. https://doi.org/10.1007/s00330-002-1734-2.

126. Magtanong, L., Ko, P.-J., To, M., Cao, J.Y., Forcina, G.C., Tarangelo, A., Ward, C.C., Cho, K., Patti, G.J., Nomura, D.K., et al. (2019). Exogenous Monounsaturated Fatty Acids Promote a Ferroptosis-Resistant Cell State. Cell Chem. Biol. *26*, 420–432.e9. https://doi.org/10.1016/j.chembiol.2018.11.016.

127. Kirkby, N.S., Reed, D.M., Edin, M.L., Rauzi, F., Mataragka, S., Vojnovic, I., Bishop-Bailey, D., Milne, G.L., Longhurst, H., Zeldin, D.C., et al. (2015). Inherited human group IVA cytosolic phospholipase A2 deficiency abolishes platelet, endothelial, and leucocyte eicosanoid generation. Faseb J.

29, 4568–4578. https://doi.org/10.1096/fj. 15-275065.

128. Newman, J.W., Watanabe, T., and Hammock, B.D. (2002). The simultaneous quantification of cytochrome P450 dependent linoleate and arachidonate metabolites in urine by HPLC-MS/MS.

J. Lipid Res. *43*, 1563–1578. https://doi.org/ 10.1194/jlr.D200018-JLR200.

129. Boutaud, O., Aronoff, D.M., Richardson, J.H., Marnett, L.J., and Oates, J.A. (2002). Determinants of the cellular specificity of acetaminophen as an inhibitor of prostaglandin H2 synthases. Proc. Natl.

Acad. Sci. USA *99*, 7130–7135. https://doi. org/10.1073/pnas.102588199.

130. Folch, J., Lees, M., and Stanley, G.S. (1957). A simple method for the isolation and purification of total lipides from animal tissues. J. Biol. Chem. *226*, 497–509. https:// doi.org/10.1016/S0021-9258(18)64849-5.

STAR★METHODS

KEY RESOURCES TABLE

REAGENT or RESOURCE	SOURCE	IDENTIFIER
Antibodies		
Rabbit anti VE-Cadherin antibody	Abcam	Cat#ab33168; RRID:AB_870662
Alexa Fluor 488 Goat anti-Rabbit IgG antibody	Invitrogen	Cat#A-11008; RRID:AB_143165
Rabbit anti-TRPV4 (extracellular) antibody	Alomone Labs	Cat#ACC-124; RRID:AB_2340915
Alexa Fluor 568 Goat anti-Rabbit IgG antibody	Abcam	Cat#ab175471; RRID:AB_2576207
GFP-NanoAntibody	Allele Biotechnology	Cat#ABP-nAb-GFPA
Monoclonal ANTI-FLAG M2 antibody	Sigma	Cat#F3165; RRID:AB_259529
Monoclonal Anti-Green Fluorescent Protein (GFP) antibody	Sigma	Cat#G1546; RRID:AB_1079024
Chemicals, peptides, and recombinant proteins		
CFTRinh-172	Sigma	Cat#C2992
Calpastatin	Sigma	Cat#208902
S1PL-IN-31	Aobious	Cat#AOB31664
HC067047	Tocris	Cat#4100
GSK1016790A	Tocris	Cat#6433
7-Amino-4-Chloromethylcoumarin, t-BOC-L-Leucyl-L-Methionine amide (CMAC, t-BOC-Leu-Met)	ThermoFisher	Cat#A6520
GsMTx-4	Alomone Labs	Cat#STG-100
Calcium Ionophore A23187	Sigma	Cat#C7522
Yoda1	Tocris	Cat#5586
Chelex-100	Sigma	Cat#C7901-25G
Tezacaftor (VX661)	MedChemExpress	Cat#HY-15448
Elexacaftor (VX445)	MedChemExpress	Cat#HY-111772
Rhodamine phalloidin	Cytoskeleton	Cat#PHDR1
Arachidonic acid	Sigma	Cat#A3611-10MG
Eicosapentaenoic acid	Sigma	Cat#E2011-10MG
Arachidonic acid alkyne	Cayman Chemicals	Cat#10538
Eicosapentaenoic acid alkyne	Cayman Chemicals	Cat#16704
Azide-fluor 488	Sigma	Cat#760765-1MG
WT-CFTR	Yarlagadda et al.[119]	N/A
ΔF508 CFTR	Yarlagadda et al.[119]	N/A
Flag-WT-CFTR	Yarlagadda et al.[119]	N/A
mPiezo1-IRES-eGFP	Coste et al.[120]	Addgene Cat#80925; RRID:Addgene_80925
PIEZO1-sYFP2	Chuntharpursat-Bon et al.[121]	N/A
TMEM16A	Karl Kunzelmann Lab	N/A
SLC26A9	RESOLUTE Consortium & Giulio Superti-Furga Lab	Addgene Cat#132140; RRID:Addgene_132140
pcDNA3.1	Invitrogen	Cat#V79020
Critical commercial assays		
Lipofectamine RNAiMax	ThermoFisher	Cat#13778150
Lipofectamine 3000	ThermoFisher	Cat#L3000015

Continued

REAGENT or RESOURCE	SOURCE	IDENTIFIER
μ-Slide VI 0.4 Ibitreat surface modification	Ibidi	Cat#80606
Fluo-8	Abcam	Cat#ab112129
Click-&-Go Cell Reaction Buffer Kit	Click Chemistry Tools	Cat#1263
Ambion miRNA Isolation Kit	Invitrogen	Cat#AM1561
Apoptosis/Necrosis Assay Kit (blue, green, red)	Abcam	Cat#ab176749
Membrane Fluidity Kit	Abcam	Cat#ab189819
Deposited data		
RNA-sequencing data	Gene Expression Omnibus database	Accession numbers: GSE244214
Experimental models: Cell lines		
Primary Human Lung Microvascular Endothelial Cells	Lonza	Cat#CC-2527
HEK-293	ATCC	Cat# CRL-1573
Recombinant DNA		
Silencer Select Human CFTR siRNA	ThermoFisher	Cat#4392420/Assay ID:s534180
Silencer Select Negative Control siRNA	ThermoFisher	Cat#4390843
Software and algorithms		
Fiji (ImageJ)	Schindelin et al.[122]	N/A
LC Pro plugin	Michael Francis	https://imagej.nih.gov/ij/plugins/lc-pro/index.html
Database for Annotation, Visualization and Integrated Discovery (DAVID)	Laboratory of Human Retrovirology and Immunoinformatics (LHRI)	https://david.ncifcrf.gov/tools.jsp
GraphPad Prism 9	Graphpad software, Inc	N/A
Adobe Illustrator	Adobe	N/A
Excel	Microsoft	N/A
PowerPoint	Microsoft	N/A
BioRender	BioRender	N/A
R Studio	Posit	N/A
BaseSpace	Illumina	N/A
QIAGEN Ingenuity Pathway Analysis	Qiagen	N/A

RESOURCE AVAILABILITY

Lead contact

Further information and requests for resources and reagents should be directed to the lead contact, AP Naren (APNaren@cshs.org).

Materials availability

- This study did not generate new unique reagents.

Data and code availability

- Bulk RNA sequencing data have been deposited at NCBI's GEO Database and are publicly available as of the date of publication. Accession numbers are listed in the key resources table.
- This paper does not report original code.
- Any additional information required to reanalyze the data reported in this paper is available from the lead contact upon request.

EXPERIMENTAL MODEL AND STUDY PARTICIPANT DETAILS

Primary cells

HMVEC-L

HMVEC-L from male and female donors (Lonza, Cat#CC-2527) were cultured in EGM-2 Bulletkit Culture Medium with supplements (Lonza, Cat#CC-3162) at 37°C and 5% CO_2. Culture media bottle was supplemented with 1% penicillin-streptomycin (Gibco, Cat#15-140-163) and

1 mL plasmocin prophylactic (InvivoGen, Cat#ant-mpp). Cells were authenticated by quality control testing and tested for mycoplasma contamination by manufacturer.

Cell line
HEK-293 cells

HEK-293 (ATCC, Cat#CRL-1573) cells were maintained in DMEM/F-12 culture medium (Invitrogen, Cat#11330) supplemented with 5% FBS (Sigma, Cat#12103C), 1% penicillin-streptomycin (Gibco, #15-140-163) and 1 mL plasmocin prophylactic (InvivoGen, Cat#ant-mpp) at 37°C and 5% CO_2. Cells were authenticated by short tandem repeat (STR) profiling and tested for mycoplasma contamination by manufacturer.

Human subjects
CF patients

In a pilot study approved by and conducted at Cincinnati Children's Hospital Medical Center, 40 CF patients (age 14.47 ± 4.16 years, 53% female, 100% white) with a range of FEV1% predicted between 27%-121% had CT scans of the lungs at a baseline clinical condition without symptoms of pulmonary exacerbation. Subjects were categorized based on the following FEV1% predicted criteria. Normal = FEV1% ≥ 100 (n = 10), mild lung disease = FEV1% =80-99 (n = 9), Moderate lung disease = FEV1% 60-79 (n = 10) and severe = FEV1% = < 60 (n = 11). There was a significant sociation between the decline in the blood volume in small blood vessels expressed as percent of total lung blood volume after adjustment for age, body mass index (BMI) and gender. Neither BMI nor gender were significant variables in the model. Informed consent was obtained from all subjects.

METHOD DETAILS
Computerized Tomography

CT exams were performed on a Canon Aquilion ONE (Canon Medical Systems Corporation, Tochigi, Japan) 320-detector CT scanner utilizing our standard high resolution CT protocol. All exams were performed without sedation or the use of contrast. Exams were acquired in volumetric mode with low dose technique utilizing 100 kV (120 kv for > 70 kg pt), 11-170 mAs. Volumetric acquisition was obtained at full inspiration and expiration, approximating total lung capacity and functional residual capacity as close as possible. Images were reconstructed in the axial plane using the "body standard volume" reconstruction kernel with lung window settings, slice thickness of 0.5 mm, and slice increment of 0.3 mm.

Pulmonary vascular morphometry

Vascular morphometry was extracted from volumetric computerized tomography (CT) scans of the chest at maximum inspiration. Feature detection algorithms such as scale-space particles methodology were used to detect vessels, which appear as intensity ridge lines on CTs and mathematically defined by the Hessian (second order derivatives) eigenvectors.[123,124] Three-dimensional physical space of the volumetric CT domain was expanded to a fourth dimension of scale for computational purposes. This four-dimensional computational domain was initialized with particles along three spatial axes and scale axis. The particles were iteratively moved along the intensity ridge lines until the system energy was minimized. This approach was applied separately for each lung independently and after resampling CT data with isotropic voxel size of 0.5mm. Vessel centerlines were identified by the strength of the intensity ridge lines in the CTs. Vascular radii were analytically estimated based on the value of the scale in the four-dimensional domain at each point along vessel center lines. Total blood vessel volume (TBV) and small blood vessel volume (BV5),[125] defined as the volume of all blood vessels with cross-sectional area less than 5 mm^2 were calculated for each of the patients and BV5/TBV ratio were compared across patients and controls.

Cell transfection
HMVEC-L siRNA

100,000 HMVEC-Ls per well between passage 3 and 6 were seeded on a 6-well plate (Corning, 3516) and grown for 4 days (<80% confluency). Silencer Select Human CFTR siRNA (ThermoFisher, Cat#4392420/s534180) or Silencer Select Negative Control siRNA (ThermoFisher, Cat#4390843) were transfected (40 nM siRNA final concentration) into cells using Lipofectamine RNAiMax (ThermoFischer, Cat#13778150) in EBM-2 basal medium (Lonza, Cat#CC-3156) containing no supplements according to manufacturer's protocol for 5h.[63] Transfection medium was then replaced with supplemented EGM-2 culture medium (Lonza, Cat#CC-3162). Cells were used 48h post-transfection.

HEK-293 overexpression system

HEK-293 cells were grown to 60-80% confluency in 6-well plate (Corning, Cat#3516). WT-CFTR,[119] F508del CFTR,[119] Flag-WT-CFTR,[119] mPIEZO1 (Addgene, Cat#80925), PIEZO1-sYFP2,[121] TMEM16A (kindly provided by Dr. Karl Kunzelmann, University of Regensburg, Regensburg, Germany), SLC26A9 (Addgene, Cat#132140), GFP (Addgene, Cat#74165) or pcDNA3.1 empty vector (Invitrogen, Cat#V79020) were transfected (0.5 µM for GFP, 1 µM for all other constructs) into cells using Lipofectamine 3000 (ThermoFisher, Cat#L3000015) in 3 mL Opti-MEM (Gibco, Cat#31985088) for 24h. Transfection medium was then replaced with DMEM/F-12 culture medium (Invitrogen, Cat#11330). Cells were used within 48h post-transfection.

Microfluidics studies

30 µL of culture medium containing 18,000-25,000 HMVEC-Ls between passage 3-7 were added per channel of µ-Slide VI (Ibidi, 0.4 Ibitreat surface modification, Cat#80606) and incubated at 37°C for 10 min to allow cells to attach. 60 µL of medium were then added to inlet and outlet wells. Slide was returned to incubator overnight for cells to spread and proliferate.

The following day, 10 mL of medium containing test compound(s) such as CFTRinh-172 (Sigma, Cat#C2992), Calpastatin (Sigma, Cat#208902), S1PL-IN-31 (Aobious, Cat#AOB31664), HC067047 (Tocris, Cat#4100), GsMTx-4 (Alomone Labs, Cat#STG-100), Arachidonic acid (Sigma, Cat#A3611-10MG), Eicosapentaenoic acid (Sigma, Cat#E2011-10MG), DMSO or methanol was prepared in 15 mL tubes. Medium containing appropriate test compounds was added to channels so that for each test compound, there was one flow channel and one static channel for control. Inlet and outlet wells of flow channels were filled to their maximum volume to prevent air gaps once connected to tubing.

Flow channels were connected to digital peristaltic pump (VWR, Cat#MFLX78001-72) inside incubator (37°C and 5% CO_2) using 2.06 mm 3-stop pump tubing (VWR, Cat#96461-42) and tube adapter set (Ibidi, Cat#10831). To set up on automated microscope (Lionheart FX, Agilent BioTek) for live recording, PVC-tubing (ThermoFisher, Cat#14-387-345) was used for extension. Tubing was completely primed with medium as to remove any air and to prevent air bubble formation. Incubator and gas-injector on automated microscope were used to maintain standard cell culture conditions (37°C and 5% CO_2). Static channels were covered to minimize medium evaporation.

Peristaltic pump was set to 11.83 mL/min for each channel, which corresponds to a shear stress of 15 dynes/cm^2 inside the channel of the µ-Slide VI 0.4, according to manufacturer (Ibidi). Flow was run for 24-48h. Phase-contrast images were obtained on automated microscope (Lionheart FX, Agilent BioTek). Data analysis (cell count) was performed using Fiji (ImageJ).

Calcium removal and supplementation

5 g/100 mL of Chelex-100 (Sigma, Cat#C7901-25G) was added to EGM-2 medium and gently stirred for 1h at room temperature (RT). Medium was then filtered with a vacuum filter system (Corning, Cat#CLS430758). Chelex-100-treated medium was supplemented with $CaCl_2$ (Sigma, Cat#C1016).

Calcium imaging

Automated microscope

siRNA transfected HMVEC-Ls were seeded on µ-Slide VI 0.4 as described above. The following day, cells were loaded with Fluo-8 (Abcam, Cat#ab112129) by adapting the manufacturer protocol to the microfluidic device. Briefly, loading dye solution was made by mixing (9000 µL of HHBS*X/96) + (1000 µL of Pluronic F-127*X/96) + (20 µL of Fluo-8 dye*X/96) where X is equal to the number of channels to be loaded with Fluo-8. Then, loading dye was mixed in a 1:1 ratio with HHBS. The loading mixture was added to the cells inside the microfluidic device so as to completely replace the culture medium. The cells were incubated at 37°C for 30 min in dark, then for 1h at room temperature (RT) in dark. The loading mixture was then completely exchanged with medium, and the slide mounted on automated microscope as described above. The automated microscope was set to read GFP for a total recording time of 10 min at a rate of 1 image per second. Cells were subjected to only 1 min of flow. Data analysis was performed using LC Pro plugin in Fiji (ImageJ) with a p value of 0.05.

Microplate reader

Transfected HEK-293 cells were seeded on poly-L-lysine (Sigma, Cat#P4707) coated 96-well optical black plate (ThermoFisher, #165305) at 80,000 cells per well in 100 µL DMEM/F-12 medium containing no FBS and no P/S overnight. The following day, cells were loaded with Fluo-8 (Abcam, Cat#ab112129) according to manufacturer protocol. Briefly, loading dye solution was made by mixing (9000 µL of HHBS*X/96) + (1000 µL of Pluronic F-127*X/96) + (20 µL of Fluo-8 dye*X/96) where X is equal to the number of wells to be loaded with Fluo-8. Then, loading dye was mixed in a 1:1 ratio with DMEM/F-12 containing no FBS and no P/S. 100 µL of loading mixture was added to each well. The cells were incubated at 37°C for 30 min in dark, then for 1h at room temperature in dark (RT). No washes were done after incubation. 50 µL of 5X Yoda1 (Tocris, Cat#5586) at final concentration 25-50 µM or DMSO was added to cells and plate was immediately read at Ex/Em = 490/525 nm on a microplate reader (FlexStation 3, VWR; or Synergy Neo2, Agilent BioTek).

Calpain activity assay

siRNA transfected HMVEC-Ls were seeded on µ-Slide VI 0.4 as described above. The following day, the slide was mounted on the automated microscope as described above. 10 µM of 7-Amino-4-Chloromethylcoumarin, t-BOC-L-Leucyl-L-Methionine amide (CMAC, t-BOC-Leu-Met, ThermoFisher, Cat#A6520) was added to the 15 mL tubes to be used to apply flow, but none to the medium inside the channels of the chip. This was important as CMAC, t-BOC-Leu-Met would immediately get cleaved by calpain and give off blue fluorescence[42] if added before recording. It was also crucial that after priming the tubing with the media containing CMAC, t-BOC-Leu-Met, the tubing was connected to the chip so as to not introduce any CMAC, t-BOC-Leu-Met in the channel until after recording has started. The automated microscope was set to read DAPI for a total recording time of 15 min at a rate of 1 image per second. The channels should not be displaying significant fluorescence at the start of recording. Cells were subjected to continuous flow for the duration of recording. Data analysis was performed using LC Pro plugin in Fiji (ImageJ) with a p value of 0.05.

Fluorescence Microscopy

Adherens junctions staining

HMVEC-Ls on µ-Slide VI 0.4 were washed 3 times with PBS (Invitrogen, Cat#10010) and fixed with 4% paraformaldehyde (Sigma, Cat#252549-500ML) diluted in PBS, for 10 min at RT. Samples were then washed again 3 times with PBS and permeabilized for 30 min at RT using 10X Permeabilization Buffer (Invitrogen, Cat#00-8333-56) diluted 1:10 in double distilled water. Samples were blocked in 2.5% normal goat serum (Vector Laboratories, Cat#S-1012-50) for 1h at RT and then incubated with primary Rabbit anti VE-Cadherin antibody (Abcam, Cat#ab33168) diluted 1:1000 in antibody diluent buffer (Epredia, Cat#TA-125-ADQ), at 4°C overnight. The next day, samples were washed 3 times for 10 min each on side-to-side shaker with PBS + 0.05% Tween-20 (Sigma, Cat#P9416-100ML) before being incubated with Alexa Fluor 488 Goat anti-Rabbit IgG antibody (Invitrogen, Cat#A-11008) diluted 1:1000 in PBS, for 1h at RT. Samples were then washed 3 times for 10 min each on side-to-side shaker with PBS + 0.05% Tween-20 and incubated with DAPI solution (ThermoFisher, Cat#62248) diluted 1:1000 in PBS, for 5 min at RT. Samples were mounted in vectashield antifade mounting media (Vector Laboratories, Cat#H-1000) and imaging was performed using a fluorescence microscope (Olympus FV1200).

TRPV4 extracellular staining

Staining of HMVEC-Ls was performed exactly as for adherens junctions but permeabilization step was omitted and samples were incubated with primary rabbit anti-TRPV4 (extracellular) antibody (Alomone labs, Cat#ACC-124) diluted 1:50.

F-actin staining and directionality

HMVEC-Ls on µ-Slide VI 0.4 were stained using rhodamine phalloidin (Cytoskeleton, Cat#PHDR1) according to manufacturer's instructions. Images were obtained using a fluorescence microscope (Olympus FV1200). Directionality analysis of F-actin filaments was performed using directionality tool in Fiji (ImageJ) with local gradient orientation method.

Alkyne labeling and click chemistry

This experiment was modified from a previously described method.[126] 60,000 HMVEC-Ls in 200 µL of cell culture medium were seeded directly on the glass of a 35 mm glass bottom dish (MatTek, Cat#P35GC-1.5-14-C) and incubated at 37°C for 15 min. 1.5 mL of culture medium was then added and the cells were returned to the incubator to spread and proliferate overnight. The next day, medium was replaced with fresh medium containing 20 µM arachidonic acid alkyne (Cayman Chemicals, Cat#10538), 20 µM eicosapentaenoic acid alkyne (Cayman Chemicals, #16704) or dimethyl sulfoxide (Sigma, Cat#D2650-100ML). The cells were then cultured at 37°C for a further 2 days. Then, cells were washed 3 times with PBS (Invitrogen, Cat#10010) and fixed with 4% paraformaldehyde (Sigma, Cat#252549-500ML) diluted in PBS, for 10 min at RT. Samples were then washed again 3 times with PBS and permeabilized for 30 min at RT using 10X Permeabilization Buffer (Invitrogen, Cat#00-8333-56) diluted 1:10 in double distilled water. Samples were washed 3 times with PBS and clicked using Click-&-Go Cell Reaction Buffer Kit (Click Chemistry Tools, Cat#1263) according to manufacturer's instructions with 5 µM azide-fluor 488 (Sigma, Cat#760765-1MG) for 30 min at RT in dark on orbital shaker. Samples were then washed 5 times with PBS and blocked in 2.5% normal goat serum (Vector Laboratories, Cat#S-1012-50) for 1h at RT. Samples were then incubated with primary Rabbit Anti VE-Cadherin antibody (Abcam, Cat#ab33168) diluted 1:1000 in antibody diluent buffer (Epredia, Cat#TA-125-ADQ), at 4°C overnight in dark. The next day, samples were washed 3 times for 10 min each on orbital shaker with PBS + 0.05% Tween-20 (Sigma, Cat#P9416-100ML) before being incubated with Alexa Fluor 568 Goat anti-Rabbit IgG antibody (Abcam, Cat#ab175471) diluted 1:1000 in PBS, for 1h at RT in dark. Samples were then washed 3 times for 10 min each on orbital shaker with PBS + 0.05% Tween-20 and incubated with DAPI solution (ThermoFisher, Cat#62248) diluted 1:1000 in PBS, for 5 min at RT. Samples were mounted in vectashield antifade mounting media (Vector Laboratories, Cat#H-1000) and imaging was performed using a fluorescence microscope (Olympus FV1200).

Apoptosis/Necrosis assay

HMVEC-Ls on µ-Slide VI 0.4 were stained with Apoptosis/Necrosis Assay Kit (Abcam, Cat#ab176749) according to manufacturer's instructions. Images were obtained on automated microscope (Lionheart FX, Agilent BioTek).

Fluorescence anisotropy

siRNA transfected HMVEC-Ls were seeded on poly-L-lysine (Sigma, Cat#P4707) coated 96-well optical black plate (ThermoFisher, #165305) at 20,000 cells per well in 100 µL EGM-2 medium overnight. The following day, cells were loaded with 10 µM pyrenedecanoic acid (PDA) labeling solution from membrane fluidity kit (Abcam, Cat# ab189819) according to manufacturer protocol for 20 min at RT. Following incubation, labeling solution was removed, and cells were washed twice with medium. 100 µL of fresh medium was then added to each well and fluorescence was immediately read at Ex/Em of both 350/400 nm and 350/470 nm to detect emission of the monomers and excimers respectively, using a microplate reader (Synergy Neo2, Agilent BioTek).

RNA Extraction for Bulk-RNA sequencing

RNA from siRNA transfected HMVEC-Ls was isolated using Ambion miRNA Isolation Kit (Invitrogen, Cat#AM1561) according to manufacturer's instructions. Samples were frozen and sent to the Genomics, Epigenomics and Sequencing Core at University of Cincinnati College of Medicine for analysis. General bioinformatic analysis was performed via BaseSpace SEQUENCE HUB app RNA-Seq Alignment v2.0.2 followed by RNA-Seq Differential Expression version 1.0.1. The analysis used STAR for alignment and Salmon for quantification (Transcripts Per Million, TPM), followed by DESeq2 to identify differentially expressed genes. List of significantly differentially expressed genes were submitted to the Database for Annotation, Visualization and Integrated Discovery (DAVID) to identify enriched pathways of interest.

Ingenuity pathway analysis

QIAGEN's Ingenuity® Pathway Analysis (IPA®, QIAGEN) was applied to the DEGs (347 mapped, 142 up-regulated and 205 down-regulated) in the above-described dataset to identify enriched pathways of interest.

Lipid analysis

siRNA transfected HMVEC-Ls were detached, pelleted, and resuspended in cell freezing medium (ThermoFisher, Cat#12648010) before being immediately snapped frozen in liquid nitrogen. Samples were sent to the Eicosanoid Core Laboratory at Vanderbilt University Medical Center for analysis. AA and EPA levels were determined by liquid-chromatography tandem mass spectrometry as previously described.[127–130]

Patch clamping

HEK293 cells were co-transfected with plasmids encoding mPIEZO1 (Addgene, Cat#80925) and WT-CFTR[119] or F508del CFTR,[119] respectively, for 24 hours using Lipofectamine 3000 (ThermoFisher, Cat#L3000015). F508del CFTR[119] was corrected with combination of 2 μM each of CFTR correctors VX445 (MedChemExpress, Cat#HY-111772) and VX661 (MedChemExpress, Cat#HY-15448)[107] in culture medium 24h prior to experiment. SLC26A3 (Addgene, Cat#132140) or TMEM16A (kindly provided by Dr. Karl Kunzelmann, University of Regensburg, Regensburg, Germany) expression plasmids were also used for comparison with WT-CFTR. Co-transfection of GFP-expression plasmid (Addgene, Cat#74165) was performed for positive selection. Whole cell patch clamp recordings were performed using an Axopatch-200B amplifier connected to Axon DigiData 1550B (Molecular Devices, CA, USA). Patch pipettes with resistances of 3 - 6 MΩ after being filled with pipette solution were prepared using a micropipette puller (Sutter Instrument, CA, USA, Cat# P-1000). To simultaneously obtain current traces at -60mV and I/V curves of CFTR, whole-cell currents were consecutively recorded with a 1 s voltage ramp of $\pm$ 100 mV applied every 10 s: hold at Vm = - 60 mV and filtered at 1 kHz and sampled at 50 Hz. The pipette solution was composed of (in mM): 133 CsCl, 5 ethylene glycol tetraacetic acid (EGTA), 1 CaCl$_2$, 1 MgCl$_2$, 10 HEPES, 0.4 GTP and 4 MgATP, titrated to pH 7.3 with CsOH. Bath solution was composed of (in mM): 127 NaCl$^-$, 3 KCl$^-$, 2.5 CaCl$_2$, 1 MgCl$_2$, 10 Glucose, 10 HEPES titrated to pH 7.3 with NaOH.[120] Yoda1 (Tocris, Cat#5586) was also made as a 10 mM stock solution dissolved in DMSO and was diluted to 10 μM final concentration in the bath solution. To obtain brief and robust Yoda1-induced Piezo1 currents, we used VCS-6_Perfusion valve system (Warner Instruments, Cat#643088) where mechanical pressure can be applied using a system for carrying out large bath volumes and fast perfusion rates at the same time, which had a similar effect such like a mechanical pressure driven by a piezoelectric-driven glass probe.[51]

Co-immunoprecipitation

HEK 293 cells co-expressing Flag-WT-CFTR[119] and PIEZO1-sYFP2[121] and HEK-293 cells expressing Flag-WT-CFTR[119] and pcDNA3.1 empty vector (Invitrogen, Cat#V79020) were lysed in lysis buffer (1x PBS, containing 0.2% Triton-X-100 and protease inhibitors phenylmethylsulfonyl fluoride 1 mM, pepstatin-A 1 μg/ml, leupeptin 1 μg/ml, aprotinin 1 μg/ml), and the clear supernatant was subjected to immunoprecipitation using GFP-NanoAntibody (Allele Biotechnology, Cat#ABP-nAb-GFPA). The immunoprecipitated complex was eluted with 100 mM glycine (pH 2.2) and quickly neutralized with 150 mM Tris (pH 8.8). The eluted proteins were mixed with sample buffer (5X; containing 1% β-mercaptoethanol), denatured, subjected to SDS-PAGE, transferred to PVDF membrane, and immunoblotted using anti-Flag antibody (Sigma, Cat#F3165) to detect CFTR and anti-GFP antibody to detect PIEZO1 (Sigma, Cat#G1546).

Tube formation assay

Wells of a 24-well plate (Corning, Cat#3526) were coated with 300 μL of Matrigel (Corning, Cat# 354234). The coated plate was incubated for 10 min at RT and for 30 min at 37°C. 250 μL of culture media containing 2X concentration of test compounds were added per well. HMVEC-Ls between passage 3 and 5 were then detached, pelleted, and resuspended at a concentration of 400,000 cells/mL. 250 μL of cell suspension were added to each test well. Images were obtained on automated microscope (Lionheart FX, Agilent BioTek).

QUANTIFICATION AND STATISTICAL ANALYSIS

Quantification for each assay is described in the method details section. Data are shown as mean ± SD and are representative of at least two independent experiments. N values depict number of technical replicates, which are described in the figure legends. All statistical analyses were performed on GraphPad Prism 9. Significance of data in flow studies was tested by two-way ANOVA if only two groups, or by two-way ANOVA with Tukey's multiple comparison if more than two groups. Significance of data on Figure 5J was tested by two-way ANOVA. Significance of all other data was tested by student t-test or by one-way ANOVA with Tukey's multiple comparison when comparing all groups with one another; or with Dunnett's multiple comparison when comparing all groups to a control group. A p value <0.05 was deemed significant. Significant differences between groups were indicated as: $*p \leq 0.05$; $**p \leq 0.01$; $***p \leq 0.001$; $****p \leq 0.0001$.